AGU PUBLICATIONS

JGR

Journal of Geophysical Research: Atmospheres

RESEARCH ARTICLE
10.1002/2015JD023520

Key Points:
- Covariance of cloud properties and sea ice depends upon atmospheric state
- Regional meteorology and sea ice alias into domain-averaged covariance
- A weak magnitude covariance is found between sea ice and cloud properties

Correspondence to:
P. C. Taylor,
patrick.c.taylor@nasa.gov

Citation:
Taylor, P. C., S. Kato, K.-M. Xu, and M. Cai (2015), Covariance between Arctic sea ice and clouds within atmospheric state regimes at the satellite footprint level, *J. Geophys. Res. Atmos., 120*, 12,656–12,678, doi:10.1002/2015JD023520.

Received 14 APR 2015
Accepted 1 DEC 2015
Accepted article online 7 DEC 2015
Published online 28 DEC 2015

Covariance between Arctic sea ice and clouds within atmospheric state regimes at the satellite footprint level

Patrick C. Taylor[1], Seiji Kato[1], Kuan-Man Xu[1], and Ming Cai[2]

[1]NASA Langley Research Center, Climate Science Branch, Hampton, Virginia, USA, [2]Department of Earth, Ocean and Atmospheric Science, Florida State University, Tallahassee, Florida, USA

Abstract Understanding the cloud response to sea ice change is necessary for modeling Arctic climate. Previous work has primarily addressed this problem from the interannual variability perspective. This paper provides a refined perspective of sea ice-cloud relationship in the Arctic using a satellite footprint-level quantification of the covariance between sea ice and Arctic low cloud properties from NASA A-Train active remote sensing data. The covariances between Arctic low cloud properties and sea ice concentration are quantified by first partitioning each footprint into four atmospheric regimes defined using thresholds of lower tropospheric stability and midtropospheric vertical velocity. Significant regional variability in the cloud properties is found within the atmospheric regimes indicating that the regimes do not completely account for the influence of meteorology. Regional anomalies are used to account for the remaining meteorological influence on clouds. After accounting for meteorological regime and regional influences, a statistically significant but weak covariance between cloud properties and sea ice is found in each season for at least one atmospheric regime. Smaller average cloud fraction and liquid water are found within footprints with more sea ice. The largest-magnitude cloud-sea ice covariance occurs between 500 m and 1.2 km when the lower tropospheric stability is between 16 and 24 K. The covariance between low cloud properties and sea ice is found to be largest in fall and is accompanied by significant changes in boundary layer temperature structure where larger average near-surface static stability is found at larger sea ice concentrations.

1. Introduction

The observed rapid Arctic surface temperature warming [*Rigor et al.*, 2000; *Chylek et al.*, 2009] and sea ice melt [*Stroeve et al.*, 2007; *Comiso et al.*, 2008] are evidence of a significant change in the Arctic surface climate. Arctic sea ice decline is a symptom and a driver of Arctic climate change [*Manabe and Wetherald*, 1975; *Holland and Bitz*, 2003; *Wang and Key*, 2003; *Hall*, 2004; *Serreze and Barry*, 2011; *Taylor et al.*, 2011a, 2011b; *Taylor et al.*, 2013; *Sejas et al.*, 2014; *Pistone et al.*, 2014]. Observations and modeling studies suggest that low clouds respond to variations in Arctic sea ice extent [*Pinto*, 1998; *Kay and Gettelman*, 2009; *Kay et al.*, 2010; *Palm et al.*, 2010; *Barton and Veron*, 2012]. Arctic low clouds—through their significant impact on the Arctic energy budget—play an important role in the Arctic climate system [*Curry et al.*, 1996; *Shupe and Intrieri*, 2004; *Kay et al.*, 2008; *Cesana et al.*, 2012; *Kay and L'Ecuyer*, 2013]. Therefore, reducing the uncertainty in the Arctic cloud covariability with the changing sea ice cover is necessary for understanding present and future Arctic climate [*Curry et al.*, 1996; *Vavrus et al.*, 2009; *Taylor*, 2012].

Arctic low clouds form under both stable—warm air over a colder surface—and unstable—cold air over a warmer surface—meteorological conditions and persist under both weak large-scale ascent and descent. Climatologically, the environment of Arctic low cloud formation results from the poleward transport of warm, moist air that is radiatively and turbulently cooled to the point of saturation [*Herman and Goody*, 1976]. Upon saturation, an intricate set of physical process interactions between radiation, turbulence, and microphysics commences contributing to the maintenance of Arctic low cloud layers [*Morrison et al.*, 2012; *Solomon et al.*, 2014]. Radiative cooling at cloud top gives rise to turbulent circulations driving cloud updrafts, potentially enhancing surface evaporation, and enabling further condensation by producing in-cloud supersaturation. Additional condensation drives stronger radiative cooling reinforcing the turbulent circulation. The importance of turbulent circulations to Arctic low cloud formation and maintenance underscores a potential cloud response to Arctic sea ice loss.

Previous studies provide evidence for a covariance between clouds and sea ice in situations when the surface and cloud layer are turbulently coupled such that reduced sea ice causes more frequent low clouds with

higher liquid water content. Evidence of this relationship in fall is provided using passive [*Kato et al*., 2006] and active [*Kay and Gettelman*, 2009; *Palm et al*., 2010] satellite remote sensing cloud data sets as well as ground-based observations [*Eastman and Warren*, 2010; *Shupe et al*., 2013]. *Schweiger et al*. [2008] and *Sato et al*. [2012] additionally suggest that the fall Arctic response to sea ice melt may be characterized by an upward shift in cloud base. *Barton and Veron* [2012] demonstrate a fall cloud response to sea ice anomalies from cloud resolving model simulations over the Laptev Sea indicating more frequent and thicker low cloud under reduced sea ice. Climate modeling studies also indicate increased Arctic low cloudiness in response to reduced sea ice cover [*Vavrus et al*., 2011]. However, *Kay et al*. [2010] provide evidence that climate models may produce too strong of a cloud response to sea ice loss especially in summer.

Arctic low cloud properties and their response to environmental changes are constrained by meteorological conditions. The most robust sensitivity of Arctic low clouds to meteorological conditions is the link with the static stability of the lower troposphere [*Kay and Gettelman*, 2009; *Solomon et al*., 2011; *Barton et al*., 2012; *Li et al*., 2014]. Increased lower tropospheric stability (LTS)—defined as the difference between the 700 hPa and surface potential temperature (θ_{700} and θ_{SFC}, respectively)—corresponds to decreased cloud fraction and total cloud water and lower cloud base and top heights [*Solomon et al*., 2011; *Barton et al*., 2012]. Increased LTS reduces the mixing between the free troposphere and cloud layer resulting in reduced cloud fraction and total cloud water because the free troposphere frequently serves as a moisture source for the cloud layer [*Solomon et al*., 2011; *Morrison et al*., 2012; *Shupe et al*., 2013]. *Barton et al*. [2012] also demonstrate that the vertical distribution of Arctic low cloud fraction is sensitive to the joint distribution of LTS and midtropospheric vertical velocity. *Kay and Gettelman* [2009] suggest that the covariance between Arctic low cloud fraction and monthly mean sea ice cover is sensitive to atmospheric pressure and near-surface static stability. It is, therefore, important to consider the meteorological conditions of the cloud environment when analyzing a potential cloud response to sea ice; this approach is taken here.

Observationally based studies of Arctic sea ice-cloud interactions primarily approach the problem from the interannual variability perspective using monthly, gridded data [e.g., *Kay and Gettelman*, 2009; *Palm et al*., 2010]. Cloud processes, however, evolve on shorter time and smaller space scales. Monthly, gridded data are well suited for studying interannual variability and detecting trends, but extracting the underlying processes from these data is difficult. However, the conclusions drawn from the monthly, gridded, and the instantaneous footprint perspectives should be consistent. This paper presents a satellite footprint-level quantification of the covariance between sea ice and Arctic low cloud properties within four atmospheric regimes using high-quality, instantaneous, footprint-level active remote sensing satellite data from the NASA A-Train.

2. Data

Instantaneous cloud property and sea ice concentration (SIC) data are obtained from the Ed RalB1 CALIPSO-CloudSat-Clouds and the Earth's Radiant Energy System (CERES)-Moderate Resolution Imaging Spectrometer (MODIS) (C3M) data set extending from July 2006 through June 2010 [*Kato et al*., 2010]. C3M provides vertical profiles of cloud fraction (CF), liquid water content (LWC), and ice water content (IWC) from merged satellite radar-lidar retrievals averaged over CERES footprints, ~20 km. Footprint SIC retrievals from Special Sensor Microwave Imager (SSM/I) [*Cavalieri et al*., 1996] are also included in C3M.

The C3M cloud property vertical profile merging process collocates Cloud-Aerosol Lidar with Orthogonal Polarization (CALIOP) [*Winker et al*., 2007], CloudSat Cloud Profiling Radar (CPR) [*Stephens et al*., 2008], Clouds and Earth's Radiant Energy System (CERES) [*Wielicki et al*., 1996], and Aqua Moderate Resolution Imaging Spectrometer (MODIS) onto the CERES footprint. The C3M cloud property vertical profiles are constructed from CALIPSO version 3 vertical feature mask (VFM; 30 m vertical resolution below 8.2 km) [*Winker et al*., 2007] and the CloudSat release 04 CLDCLASS product (240 m vertical resolution) [*Sassen and Wang*, 2008]. The C3M cloud property vertical profiles have a vertical resolution of 120 m. The C3M vertical profile merges the cloud top and base heights determined separately by the VFM and CLDCLASS products. Due to the higher sensitivity and vertical resolution of CALIOP, the VFM cloud top and base heights are given precedence. CPR-derived cloud heights are used only when CALIOP does not detect a cloud or is completely attenuated [*Kato et al*., 2010]. CALIOP provides 85% and 77% of the cloud top and base heights, respectively.

Cloud optical thickness and cloud liquid and ice water amounts within C3M are derived from a combination of passive retrievals from MODIS radiances using the CERES science team Edition 3 retrieval algorithms

described in *Minnis et al*. [2011a, 2011b] and active cloud boundary retrievals from CALIPSO and CloudSat. The MODIS optical thickness retrieval is enhanced when clouds are single layer by adjusting the retrieved effective cloud top height to match that from CALIPSO and CloudSat as described in *Kato et al*. [2011]. CloudSat-derived ice and liquid water contents are converted to the extinction coefficient using the relationship given by *Fu* [1996] for ice and by *Minnis et al*. [1998] for liquid. Note that *Fu* [1996] assumes that ice crystals are hexagonal. Particle size is needed for the conversion of CloudSat radar reflectivity to IWC. If CloudSat particle size is not available, MODIS-derived particle size is used. The extinction coefficient integrated over all cloud layers in the column is normalized by the optical thickness derived by MODIS [*Kato et al*., 2011]. Ice and liquid phase discrimination is based on CloudSat derived LWC and IWC profiles partitioned using a −20°C temperature threshold.

Optical thickness, LWP, and IWP retrieval from MODIS have a large uncertainty, especially those retrieved during polar night. The uncertainty increases with increasing SIC (P. Minnis, personal communication, 2015). During summer when the solar zenith angle is higher than 82°, the Visible Infrared Shortwave-infrared Split window Technique (VISST) using the 0.6, 3.8, and 10.8 μm channels is employed over snow and ice-free surface. Over snow and ice-covered surfaces the Shortwave-infrared Infrared Near-infrared Technique is used which is similar to VISST but replaces the 0.6 μm with either the 1.6 or 2.1 μm channel [*Minnis et al*., 2011a]. When solar zenith angle is larger than 82°, the Shortwave-infrared Split-window Technique using brightness temperature differences between 3.8, 10.8, and 12.0 μm channels to retrieve cloud properties over all surfaces [*Minnis et al*., 2011a, 2011b]. Currently, there is no direct method to estimate the uncertainty in the cloud properties retrieved over sea ice during polar night because in situ observations are unavailable. Available in situ observations in other seasons show that CloudSat-retrieved IWC is found to be within 25% of in situ measurements [*Austin et al*., 2009]. *de Boer et al*. [2008] demonstrate that the CloudSat 2B-CWC-RO cloud water content product reliably compares with ground-based radar and lidar site in Eureka, Canada. Higher confidence is given to the vertical distribution of LWC and IWC than in the absolute magnitude; therefore, emphasis in this study is on the vertical profiles. The uncertainty in C3M cloud fraction is considered to be small <0.01 when clouds are thin because CALIPSO is sensitive to clouds and can detect IWC of 0.4 mg m^{-3} and 0.1 mg m^{-3} during day and night, respectively [*Avery et al*., 2012].

An indirect method of estimating uncertainty in the cloud properties retrieved over sea ice during polar night using radiative closure is available. Figure 2 in *Kato et al*. [2011] indicates that using CALIPSO and CloudSat-derived cloud properties significantly improves the agreement of computed top of the atmosphere (TOA) longwave irradiance with CERES over the Arctic in January and July. The method described above is used in these computations. This result indicates that once CF and cloud top and base heights are constrained by CALIPSO and CloudSat, MODIS-derived cloud properties are probably not the dominant source of error for modeling TOA irradiances. An unresolved issue is whether this uncertainty is small enough to detect the dependence on SIC.

Conclusions within this study are based upon the average cloud property changes with varying SIC; systematic biases in the cloud property retrievals do not impact the results. While retrieved cloud properties from passive sensors are affected by SIC, active sensor retrievals, especially CALIOP, are considered to be insensitive to SIC. Some sea surface state-dependent uncertainty, however, is possible in C3M data due to the vertical profile merging process. If there is a dependence of cloud optical depth on SIC, CALIOP will attenuate more at lower SIC, and the CPR-derived cloud base height will be used more frequently in these scenes. More confidence is given to the high-resolution, CALIOP-derived cloud base heights because the CPR has surface clutter below ~1.2 km [*Marchand et al*., 2008] due to strong surface reflections. To test the effect of CALIPSO signal attenuation, a sensitivity study is performed as part of this study using only footprints when the CALIOP signal reaches the ground. This sensitivity study indicates that the C3M cloud property and SIC covariance are generally insensitive to the degree of CALIOP attenuation and does not significantly influence the conclusions.

Sea ice concentration (SIC) is defined as the areal coverage of sea ice within the instantaneous instrument footprint. SIC is retrieved from passive microwave radiometer satellite data record using the Special Sensor Microwave/Imager (SSM/I) for 2006–2007 and Special Sensor Microwave Imager/Sounder (SSMIS) for 2008 to present using the revised NASA team algorithm [*Cavalieri et al*., 1996]. The SIC data set resolution is 25×25 km^2 and are available daily. Accuracy of SIC is reported to be ±5% in winter and ±15% in summer when melt ponds are present [*Cavalieri et al*., 1997; *Steffen et al*., 1992].

Table 1. Definition of Atmospheric State Regimes and Thresholds

Regime Name—Frequency of occurrence	LTS Threshold	ω_{500} Threshold
High stability (HS)—36%	16 K–24 K	> -0.1 Pa s^{-1}
Stable (S)—28%	<16 K	> -0.1 Pa s^{-1}
Very high stability (VHS)—23%	>24 K	> -0.1 Pa s^{-1}
Uplift (UL)—13%	None	< -0.1 Pa s^{-1}

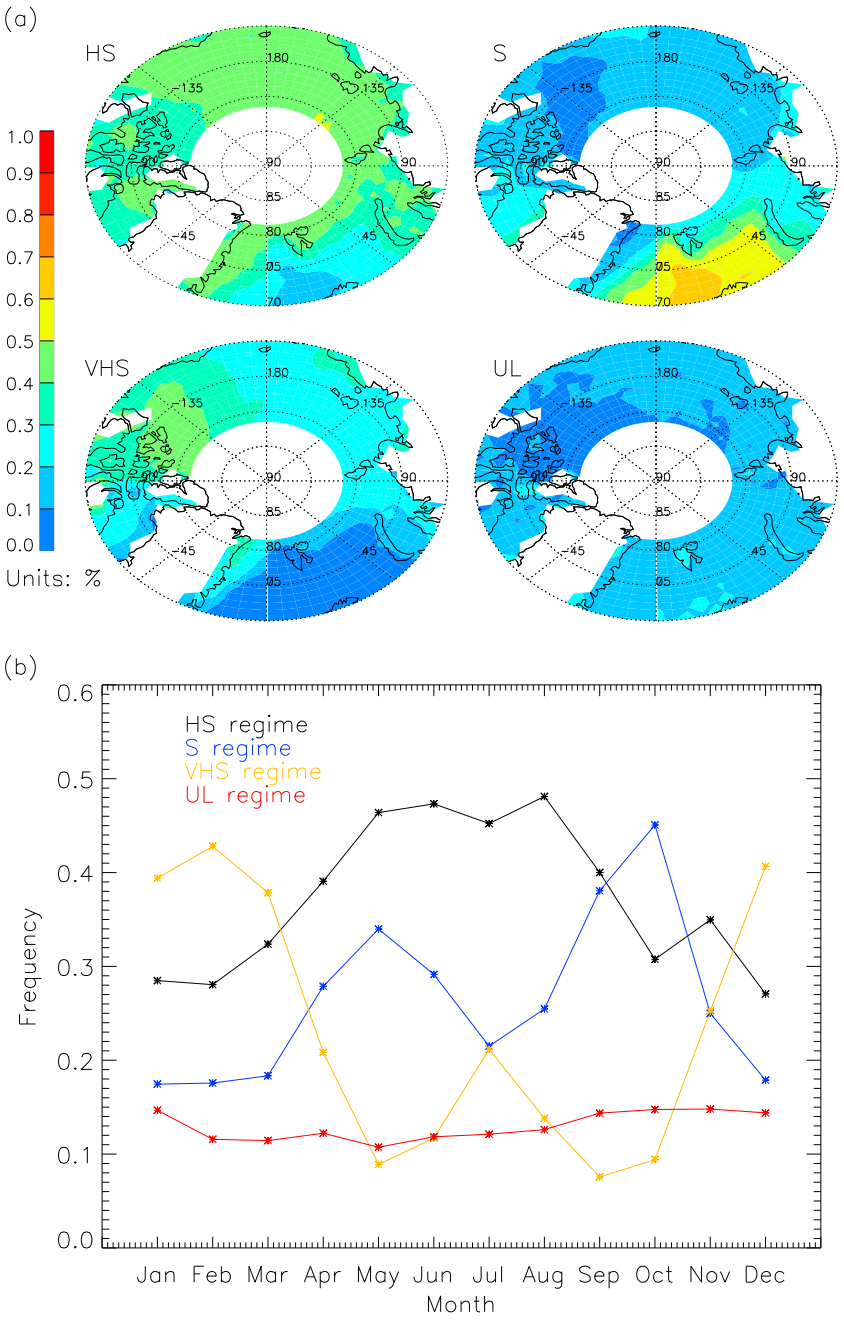

Figure 1. The (a) spatial distribution (b) annual cycle frequency distribution of the individual atmospheric state regimes for all surface types poleward of 70°N.

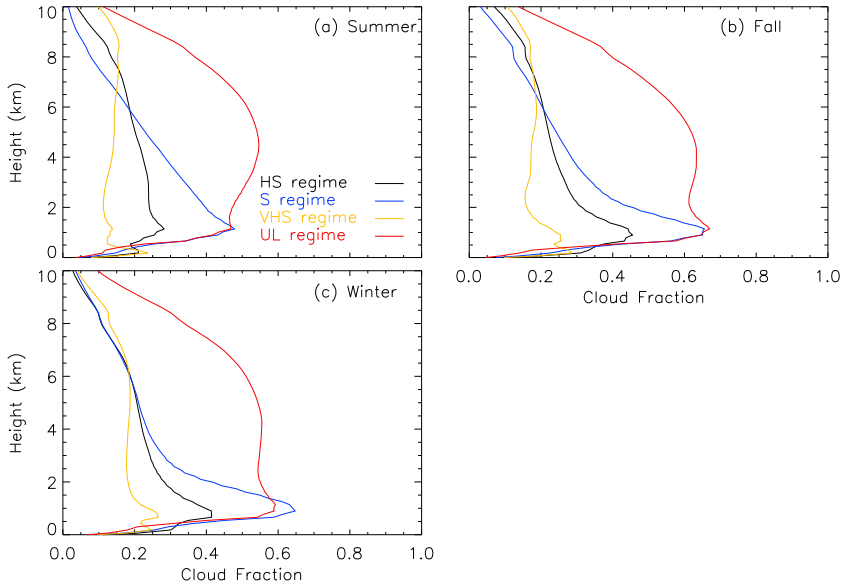

Figure 2. Average cloud fraction vertical profile for each atmospheric regime across the Arctic Ocean and sea ice areas poleward of 70°N is shown by season: (a) summer, (b) fall, and (c) winter. The *x* axis is cloud fraction, and the *y* axis is height in kilometer. The atmospheric regimes are denoted by HS (black line), S (blue line), VHS (orange line), and UL (red line).

Partitioning footprints by meteorological conditions are critical. Meteorological conditions are determined by collocating each footprint with the closest grid point in space and time from the Modern Era Retrospective analysis for Research and Applications (MERRA) [*Rienecker et al.*, 2011]. MERRA meteorological fields used are three hourly resolution on a reduced 1.25° × 1.25° grid. Because of the known large uncertainty in atmospheric state over the Arctic, ECMWF (European Centre for Medium-Range Weather Forecasting) Interim reanalysis [*Berrisford et al.*, 2011; *Dee et al.*, 2011] is used to test the sensitivity of the results to the reanalysis data set. Despite modest instantaneous correlation (~0.5) between the 500 hPa vertical velocity (ω_{500}) and LTS of the two reanalyses, the study results are not affected by the choice of reanalysis.

3. Methodology

3.1. Atmospheric Regimes

Arctic cloud properties are to first order controlled by the meteorological conditions in which they occur [e.g., *Kay and Gettelman*, 2009; *Barton et al.*, 2012]. Therefore, the analysis must account for the dependence of cloud properties on atmospheric state. An earlier study [*Barton et al.*, 2012] separates meteorological conditions into four atmospheric state regimes using LTS and ω_{500} by applying a *k*-means cluster analysis. We adopt the LTS and ω_{500} thresholds in *Barton et al.* [2012] to account for the dependence of cloud properties on atmospheric state. Table 1 summarizes the thresholds of the four regimes: high stability (HS), stable (S), very high stability (VHS), and uplift (UL). The HS, S, and VHS regimes only differ by the LTS threshold. The UL regime is the only regime with midtropospheric rising motion and represents frontal clouds; all other regimes are characterized by weak subsidence. The spatial and annual cycle distributions of the atmospheric state regimes agree well with *Barton et al.* [2012] despite the use of a different reanalysis; Figures 1 and 2 and Table 2 are similar to *Barton et al.* [2012].

Table 2. Average Low Cloud (<3 km) Properties Within Each Atmospheric State Regime

	Summer				Fall				Winter			
	Frequency	CF[a]	LWP	IWP	Frequency	CF[a]	LWP	IWP	Frequency	CF[a]	LWP	IWP
HS	0.47	0.69	47.8	6.5	0.35	0.81	35.4	18.4	0.34	0.68	20.1	35.7
S	0.25	0.81	49.3	13.9	0.42	0.90	39.0	25.4	0.23	0.84	33.7	38.1
VHS	0.16	0.51	41.6	1.8	0.08	0.60	22.3	12.5	0.31	0.53	6.8	34.2
UL	0.12	0.77	36.8	29.8	0.15	0.89	22.4	50.0	0.12	0.82	14.8	48.7

[a]CF represents cloud fraction. Frequency of occurrence represents only the Arctic Ocean and sea ice domains. LWP and IWP units are g m^{-2}.

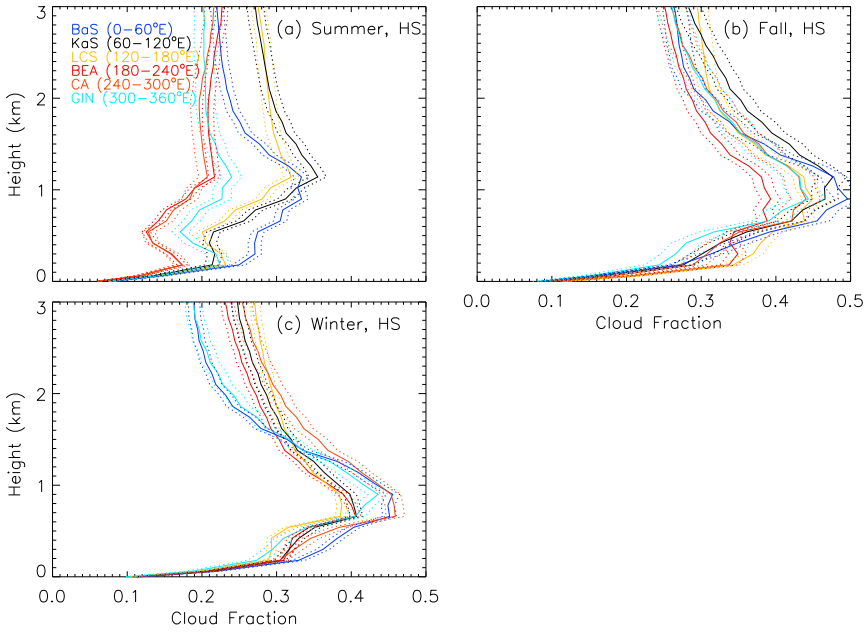

Figure 3. Average cloud fraction vertical within each of the six Arctic regions for (a) summer, (b) fall, and (c) winter of the HS atmospheric regime. Dashed lines represent the 2σ standard error around the mean.

The annual mean spatial variability of the four atmospheric state regimes across the Arctic domain is shown in Figure 1a. The frequency of occurrence each atmospheric regime is not spatially uniform. The S regime preferentially occurs on the North Atlantic storm track region of the Arctic. The HS regime occurs most frequently in the Beaufort, Chukchi, and Laptev Sea Basins. The VHS regime maximizes east of the Beaufort Sea toward the Canadian Archipelago—a region of significant multiyear sea ice [*Polyakov et al.*, 2012]. The UL regime frequency of occurrence reaches 0.2 in portions of the Arctic but exhibits weak spatial variability.

The annual mean of the spatially integrated occurrence of the four regimes varies with month. Figure 1b shows the annual cycle of each regime for the entire Arctic domain. The HS, S, and VHS regimes show a significant seasonality. The S regime frequency of occurrence annual cycle shows two peaks—late spring and early fall. The HS regime frequency of occurrence shows a maximum in summer reaching 48%. The VHS regime shows a small peak in summer but occurs most frequently in December–February reaching ~44%. The UL regime exhibits little seasonality. The lack of dependence of occurrence in the UL regime both spatially and temporally suggests that the UL regime is not strongly related to local surface properties. The strong dependence of the other regimes on location and time of year, on the other hand, suggests that local thermodynamic coupling of the atmosphere and surface may play an important role in the origins of clouds within these regimes.

The four atmospheric state regimes exhibit statistically different cloud properties and a unique vertical distribution of CF. The average, column-integrated cloud properties within each atmospheric state regime is summarized in Table 2. In addition, Figure 2 shows that the vertical profile of CF depends on atmospheric state regime and season. CF differences >0.01 are statistically significant at the 95% confidence level. For all seasons, the S, HS, and VHS regimes demonstrate a robust relationship between the CF profile and LTS where (1) total CF fraction decreases and (2) the height of maximum CF decreases with increasing LTS.

In the designation of atmospheric state regimes, LTS and ω_{500} serve as diagnostics of atmospheric state and are correlated with other atmospheric conditions that influence cloud characteristics—e.g., moisture advection, low-level vertical velocity, and near-surface stability. The relationship between LTS, ω_{500}, and other atmospheric variables varies with season and location. Despite the correlations between LTS, ω_{500}, and other atmospheric variables, significant regional variability of the cloud properties within each atmospheric regime is found (Figure 3).

The spatial and seasonal variability of the atmospheric state regimes contributes to the variability of cloud properties; however, these regimes do not explain all cloud variability. Figure 3 demonstrates the significant

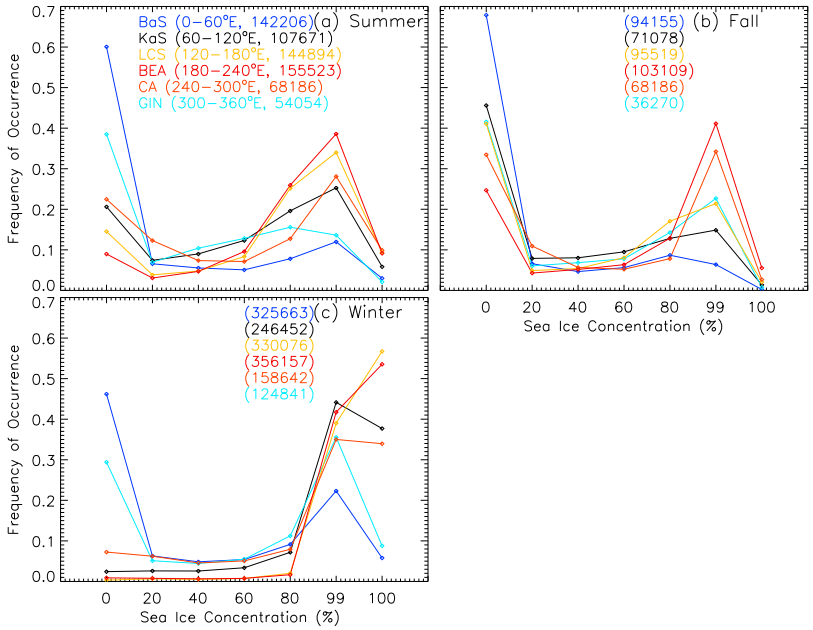

Figure 4. Regional probability distributions of sea ice concentration for each of the Arctic regions for (a) summer, (b) fall, and (c) winter. The numbers in parentheses represent the total number of satellite footprints within each region.

variation between several regions in the CF vertical profile within the atmospheric regimes. The Arctic is separated into six regions each 60° longitude in width: namely, Barents Sea (BaS; 0°–60°E), Kara Sea (KaS; 60°–120°E), Laptev-Chukchi Seas (LCS; 120°–180°E), Beaufort Sea (BEA; 180°–240°E), Canadian Archipelago (CA; 240°–300°E), and Greenland-Iceland-Norwegian Seas (GIN; 300°–0°E) regions. The regions are referred to by the names of the marginal seas or major geographic features that they contain. The BaS region exhibits the most cloudiness, which is associated with the North Atlantic Storm Track. The large regional variability of the cloud properties within these atmospheric state regimes is attributed to specific meteorological conditions within each region that generate the atmospheric state regimes. In other words, the meteorological conditions that generate the HS regime over the North Atlantic, for example, are different from those that generate the HS regime over BEA.

Barton et al. [2012] do not discuss or demonstrate any regional variations of cloud properties within atmospheric regimes. CALIOP is the only source of cloud information in *Barton et al.* [2012]. As a result of using lidar-only data, the low cloud information is regionally subset implicitly because lidar shots reach the ground much less frequently over the North Atlantic than over other Arctic regions. The inclusion of CloudSat provides low cloud information in regions where CALIOP frequently attenuates.

The regional differences in meteorology must be removed to analyze the covariance between cloud properties and SIC. The regional meteorological contributions to cloud property variations are removed by computing regional anomalies. First, average cloud properties (either vertical profile or column integrated value) are computed on a 1° latitude by 5° longitude grid within each atmospheric regime. Regional anomalies are then computed for each footprint with respect to the $1° \times 5°$ gridded average for each atmospheric state regime. The use of regional anomalies removes the influence of spatial variations in the atmospheric regimes on the cloud field. This step is also important because regional variations in the SIC distribution (Figure 4) correlates with the regional variations in the cloud characteristics and can alias into the covariance. The regional anomalies are computed for each month in order to remove as much of the seasonal meteorological influence as possible. The remaining seasonal dependence of the cloud-sea ice covariance is considered to be related to differences in surface-atmospheric coupling. All results shown are placed in absolute space by adding back in the Arctic domain averaged cloud properties for each regime.

3.2. Composite Method

A composite approach sorting and averaging instantaneous satellite footprint low cloud properties by the instantaneous SIC is adopted. Clouds with top heights below 3 km are defined as low clouds. This threshold

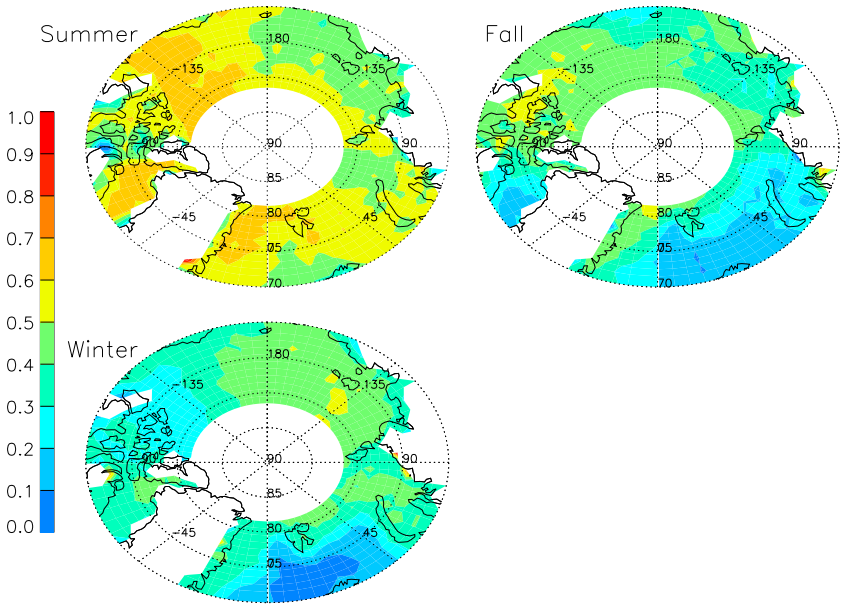

Figure 5. The spatial distribution of the HS regime frequency of occurrence for summer, fall, and winter.

definition of low cloudiness is selected to ensure that the peak in low cloudiness is captured in each profile and in all seasons. Due to the seasonal variations in cloud depth, this uniform cloud height threshold definition of low cloudiness may introduce a seasonal variation in the ratio of liquid to ice water path; this affect is considered to be small because most clouds are found near 1 km in all seasons. Additionally, the cloud fraction vertical profiles in the HS, S, and VHS regimes begin to converge above ~4 km (Figure 2).

Random error in the average cloud properties within each SIC bin is determined assuming a Gaussian distribution and computing the standard error (SE).

$$\mathrm{SE}_{i,j} = \frac{\sigma_{i,j}}{N_{e\ i,j}} \tag{1}$$

In (1), $\mathrm{SE}_{i,j}$ represents the standard error within each SIC bin i and atmospheric regime j and is given by the ratio of the cloud property standard deviation ($\sigma_{i,j}$) and the effective number of independent samples ($N_{e\ i,j}$). $N_{e\ i,j}$ is determined following *Gordon et al.* [2005] where a string of consecutive footprints falling into the same atmospheric regime is considered a single observation. All error bars shown are given by 2*SE to represent the 95% confidence interval. The average number of consecutive footprints within each regime is 10 (200 km) for the HS and S regimes, 12 (240 km) for the VHS regime, and 5 (100 km) for the UL regime. This approach is used to compute error bars. Each footprint is placed into the appropriate SIC bin using the instantaneous SIC to avoid combining footprints with very different SIC values.

Instantaneous observations of cloud properties are composited by SIC within three seasons over the ocean and sea ice areas poleward of 70°N. Seasons are defined using the spatial distribution of the atmospheric regimes. The three seasons are summer (June–August), fall (September and October), and winter (November through May). The months are assigned to seasons using the spatial correlation of the frequency of occurrence of the atmospheric regimes. For example to define fall, the spatial correlation of the atmospheric regimes in September and October exhibit higher correlations with each other than with August and November, respectively. Winter is defined as November through May because the atmospheric regime spatial distribution in November correlates more strongly with December than with October, and the atmospheric regime spatial distributions in April and May more strongly correlate with March than June. This method is used to define seasons because of the significant regional variation of the cloud properties within atmospheric regimes. The definitions of summer and fall determined in this manner are consistent with previous work [e.g., *Kay and Gettelman*, 2009]. Figure 5 demonstrates the spatial distribution of HS regime frequency of occurrence within each season.

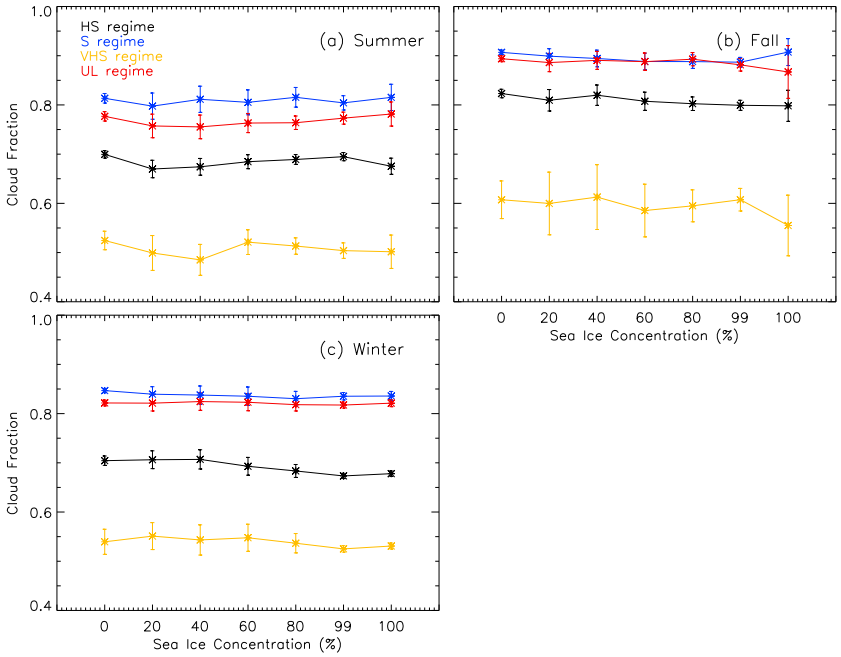

Figure 6. Average cloud fraction in the lowest 3 km composited by SIC for each atmospheric regime and season: (a) June–August (JJA), (b) September and October (SO), and (c) November–May (NDJFMAM). Error bars represent the 2σ standard error for each average. Each bin is plotted by the upper SIC limit.

The SIC composite bins are 20% in width except for scenes covered completely by ocean or sea ice; 0 and 100% SIC footprints are placed into individual bins. Cloud properties are averaged within each SIC bin. A statistically significant covariance is identified when average cloud properties between SIC bins are different at a 95% confidence level and represent the covariance magnitude that is detectable given the available sample size.

The use of instantaneous satellite footprints instead of monthly means has several advantages. Instantaneous cloud property and SIC retrievals retain processes occurring at the native time and space scales. The relationship between cloud properties and SIC that is statistically significant at an instantaneous scale might become statistically insignificant when monthly gridded values are used if atmospheric states changes significantly within a month. In addition, discretizing SIC in 20% bins can resolve possible nonlinear relationships between cloud properties and SIC. The use of a simple linear regression with monthly mean values can be misleading because it obscures such nonlinear relationships.

SIC is selected as the compositing variable because it influences the surface turbulent fluxes. Once ocean surface is frozen, surface turbulent fluxes are smaller compared to fluxes from ice-free ocean [e.g., *Boisvert et al.*, 2012]. The hypothesized link between clouds and sea ice is through a change of turbulent fluxes influencing cloud properties by changing vertical moisture transport. The overall contribution of this mechanism to the cloud layer is currently unknown. SIC is, therefore, used as a surrogate because surface turbulent flux data sets over the Arctic contain significant uncertainties [e.g., *Bourassa et al.*, 2013].

4. Results

4.1. Covariance of Column-Integrated Cloud Properties and Sea Ice Concentration

4.1.1. Cloud Fraction

Figure 6 illustrates the composite analysis for CF and SIC within each season. The error bars indicate the 2σ standard error associated with each average. The most striking feature in Figure 6 is the dependence of CF on atmospheric regime. CF increases with decreasing LTS (e.g., from VHS to S). This relationship is summarized in Table 2 and is consistent with previous work [e.g., *Solomon et al.*, 2011; *Barton et al.*, 2012].

Table 3. Summary of Statistically Significant Covariance Found Between Column-Integrated Cloud Properties and Sea Ice Concentration

	Summer	Fall	Winter
HS	CF, LWP	CF, LWP, IWP	CF, LWP
S		LWP, IWP	LWP
VHS	LWP		
UL	LWP, IWP		

The covariance between column-integrated CF and SIC is assessed after separating the influence of atmospheric regime and accounting for the variation within each atmospheric regime. Figure 6 indicates that average CF tends to be smaller in footprints with higher SIC values; however, this decrease in CF with increased SIC is weak (<0.05 from 0% to 100% SIC) and in most cases not statistically significant. The largest difference in the average CF between adjacent SIC bins is generally found between the 0% and 1–20%; the maximum value of this difference, however, reaches only 0.03 in the HS regime in summer.

The magnitude of the column-integrated CF varies across atmospheric regimes and seasons. The differences between the average column-integrated CF in the 0% and 100% SIC bins are used to provide a measure of the overall covariance of CF and SIC. In summer (Figure 6a), the average CF difference between 0% and 100% SIC is <0.01 for the S and UL regime and is 0.03 for the HS and UL regimes. In fall, the average CF difference between 0% and 100% SIC is <0.01 for the S regime but 0.03–0.05 for the other regimes. The weakest CF and SIC covariance magnitude is found in winter: <0.01 for the S, VHS, and UL regimes and 0.02–0.03 for the HS regime. These CF differences—between the 0% and 100% SIC in summer and winter and between 0% and 80–99% SIC—are statistically significant at the 95% confidence level only in the HS regime. Statistically significant relationships are summarized in Table 3.

4.1.2. Cloud Water Path

Figure 7 shows the composite analysis for liquid water path (LWP), ice water path (IWP), and total water path (TWP = LWP + IWP). LWP and IWP values are determined by integrating the LWC and IWC from the surface to 3 km. Even though the uncertainty of TWP, LWP, and IWP may be large, we analyze the dependence on atmospheric regime, SIC, and season to investigate physical plausibility of the relationship with SIC. The

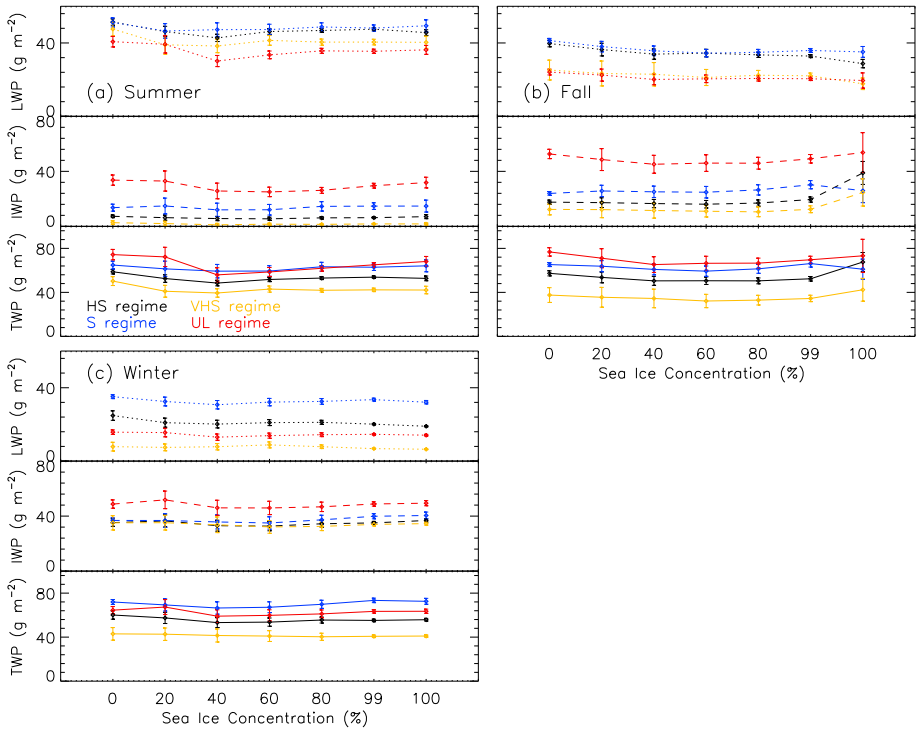

Figure 7. Average LWP (dotted lines), IWP (dashed lines), and TWP (solid lines) in the lowest 3 km composited by SIC for each atmospheric regime and season: (a) JJA, (b) SO, and (c) NDJFMAM. Error bars represent the 2σ standard error for each average. Each bin is plotted by the upper SIC limit.

differences in the footprint-averaged LWP or IWP at different SIC values (Figure 7) are smaller than the uncertainty in current passive remote sensing retrievals (P. Minnis, personal communication, 2015). The TWP, LWP, and IWP are found to increase with decreasing stability in manner physically consistent with CF.

The covariance between LWP and SIC is also consistent with the column-integrated CF results. A general tendency for smaller average LWP values at higher SIC values is found in all regimes and seasons (Figure 7). The main difference is that the average change in the LWP, on a percentage basis, are larger than those found in the average CF.

The magnitude of the differences in the average LWP with varying SIC changes with atmospheric regime and season. In summer, the overall magnitude of the covariance across atmospheric regimes, as indicated by the difference between 0% and 100% SIC bins, is 2–7 g m^{-2} (Figure 7a). The largest and only statistically significant difference, 7 g m^{-2}, is found in the HS regime. The largest average LWP differences, 3–7 g m^{-2}, in summer are found between the 0% and 20–40% SIC bins in the UL and VHS regime, smallest in the S regime. The differences between the 0% and 20–40% SIC bins are statistically significant for the all regimes except the S regime. The largest-magnitude LWP and SIC covariance is found in fall and in the HS regime; the difference exceeds 10 g m^{-2} and is statistically significant. All other regimes in fall show a difference in average LWP of 5–7 g m^{-2} but are not statistically significant. The magnitude of the covariance between LWP and SIC in winter is weakest and ranges from 0 to 5 g m^{-2}. The only regime that exhibits statistically significant differences in winter is the HS regime (Table 3).

The covariance between LWP and SIC is the same magnitude as the dependence of LWP on atmospheric regime in fall. The differences in LWP between 0% and 100% SIC bins are the same magnitude as the difference between the HS to S regimes at 100% SIC. The comparison between the two regimes within a SIC bin is independent of retrieval errors due to surface type. The result suggests a different LWP and SIC covariance in fall between the HS and S regimes.

The average IWP change with SIC indicates a different behavior than LWP. Figure 7 shows the change in average IWP across the SIC bins. It is difficult to state a general change in average IWP with varying SIC, as it changes with season. The seasonal dependence in IWP is likely due to the strong seasonal variation of the average IWP. In summer, the average IWP tends to be either unchanged or slightly lower at higher SIC. In fall, the HS, S, and VHS regimes show a larger average IWP at high SIC, whereas the UL regime exhibits a "U-shaped" curve. In winter, the average IWP is found to slightly increase at higher SIC.

The magnitude of the differences in average IWP under varying SIC values is generally smaller than for LWP. In summer, the HS, S, and VHS regimes show little change $<$1 g m^{-2}; none of which are statistically significant. The average IWP difference in the UL regime between the 0% and 100% SIC bins is ~2 g m^{-2}; however, the difference between the 0% and 60–80% SIC bin reaches 5 g m^{-2} and is statistically significant. Winter also shows small differences between the 0% and 100% SIC in the average IWP between SIC bins ranging from +1 to +3 g m^{-2} for all regimes; none are statistically significant. The differences in the average IWP between 0% and 100% SIC are largest in fall, ranging from 2 to 18 g m^{-2}, and are statistically significant at the 95% confidence level in the HS regime (Table 3).

The average TWP for each SIC bin is shown for reference in Figure 7. In summer, the TWP results follow the LWP because there is much less IWP. In autumn and winter, the covariance of TWP with SIC depends on both LWP and IWP.

4.2. Covariance of Cloud Property Vertical Profiles and Sea Ice Concentration

This section discusses the compositing methodology applied to the vertical profiles of CF, LWC, and IWC. As mentioned in section 3.1, the vertical CF profile depends on atmospheric regime. CF increases with decreasing atmospheric stability for all layers below 3 km and for all seasons. Overall, the average cloud property vertical profiles for footprints of varying SIC are different at a 95% confidence level at many altitudes, under several atmospheric regimes, and in several seasons. There are too many details of the covariance between the cloud property vertical profiles and SIC to be fully discussed. Therefore, we discuss the results that illustrate the general characteristics across regimes and a few unique characteristics. The colors in these figures correspond to the SIC bins, where blue represents 0% and red represents 100% SIC.

Table 4. Summary of Statistically Significant Covariance Found Between Cloud Property Vertical Profile and Sea Ice Concentration[a]

	Summer	Fall	Winter
HS	CF (100–300 m) LWC (300 m–1.1 km)	CF (600 m–1.0 km) LWC (800 m–1.0 km)	CF (600 m–1.1 km) LWC (500 m–1.2 km)
S		CF (600 m–1.1 km) LWC (700 m–1.1 km)	CF (600 m–1.1 km) LWC (700 m–1.1 km) IWC (700 m–1.0 km)
VHS			
UL	LWC (600 m–1.2 km)	CF (500 m–1.0 km)	

[a]Values in parentheses describe the height range in which the statistically significant covariance is found.

4.2.1. Vertical Cloud Profile

Statistically significant differences between the average CF vertical profiles under varying SIC are found within several atmospheric regimes and seasons. The statistically significant cloud property vertical profile results are summarized in Table 4. The overall covariance between the average CF vertical profile and SIC for all atmospheric regimes and seasons is characterized by a decrease in the average CF from 0% to 60% SIC, after which average CF increases at many altitudes. This behavior is found in most regimes and seasons; however, the magnitude of the CF covariance with SIC differs. All statistically significant differences indicate a smaller average CF at larger SIC values; in no case is the increase in CF at SIC >60% statistically significant. For most regimes, statistically significant differences in the average CF are found between the 0% and 20–40% SIC and/or the 0% and 40–60% SIC bins; therefore, 2σ error bars are only shown for these SIC bins in Figures 8–13 when statistically significant differences are found. Statistically significant differences are found most often between 500 m and 1.2 km, and the largest CF changes are found at the height of the maximum value.

The overall magnitude of the differences in the average CF vertical profile is always less than 0.1. The magnitude of the average CF covariance with SIC is quantified as the difference between 0% and 20–40% SIC bins because of the general CF increase at SIC >60%. The magnitude of the average CF differences at the level of maximum is similar in magnitude for all atmospheric regimes (0.02–0.07) but is largest for the HS and S and

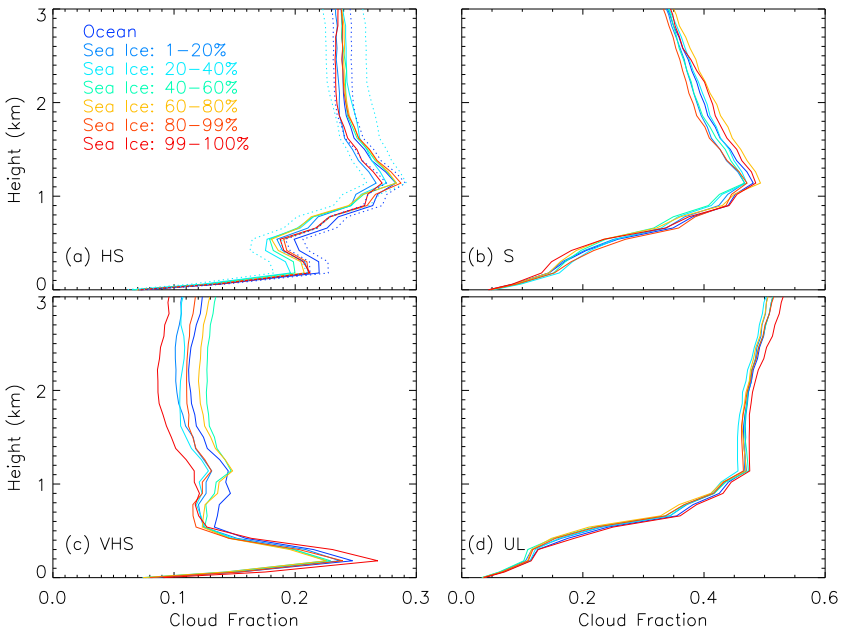

Figure 8. Summer season composite analysis applied to the CF vertical profile for the (a) HS, (b) S, (c) VHS, and (d) UL regimes. Dashed lines represent the error and are the 2σ standard error for the average at each height. Error bars are only shown in cases where statistically significant differences are found.

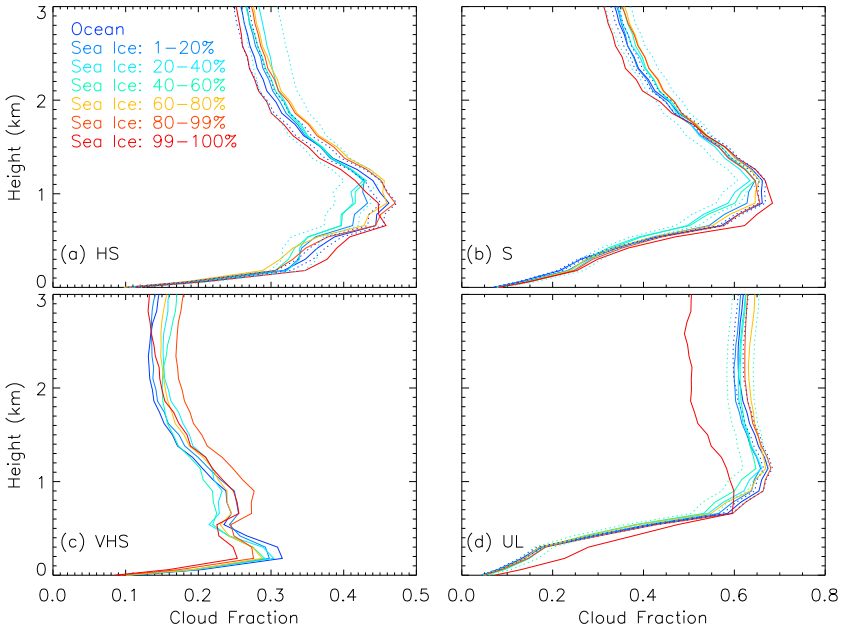

Figure 9. Fall season composite analysis applied to the CF vertical profile for the (a) HS, (b) S, (c) VHS, and (d) UL regimes. Dashed lines represent the error and are the 2σ standard error for the average at each height. Error bars are only shown in cases where statistically significant differences are found.

weakest for the UL regime. The largest differences in the average CF in summer are found close to the surface between 100 and 300 m in the HS regime and reach 0.03 (Figure 8). Fall (Figure 9) and winter (Figure 10) exhibit larger differences in the average CF in the HS and S regimes reaching 0.05 between 600 and 900 m. Seasonally, the largest difference between the 0% and 20–40% SIC bins is found between 500 m and 1.2 km in fall and in the HS regime.

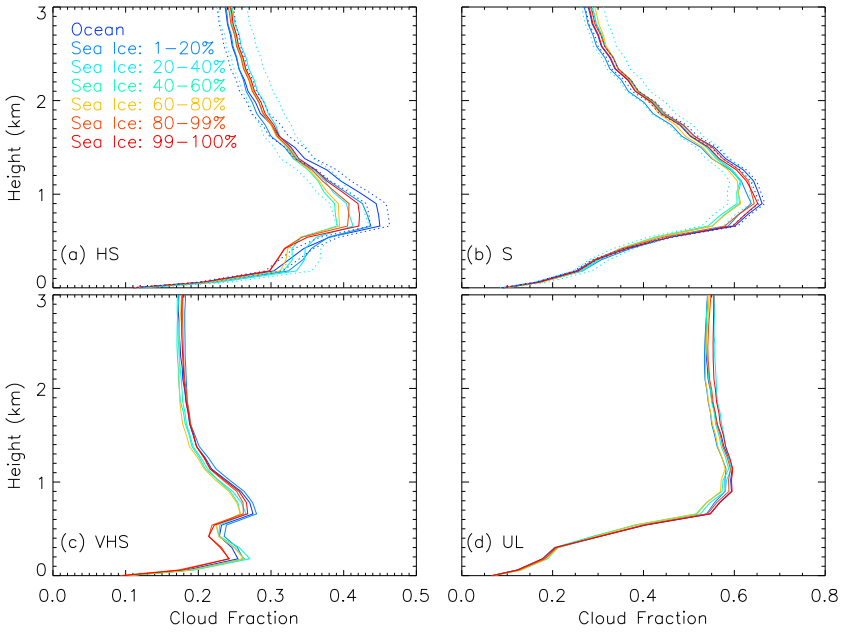

Figure 10. Winter season composite analysis applied to the CF vertical profile for the (a) HS, (b) S, (c) VHS, and (d) UL regimes. Dashed lines represent the error and are the 2σ standard error for the average at each height. Error bars are only shown in cases where statistically significant differences are found.

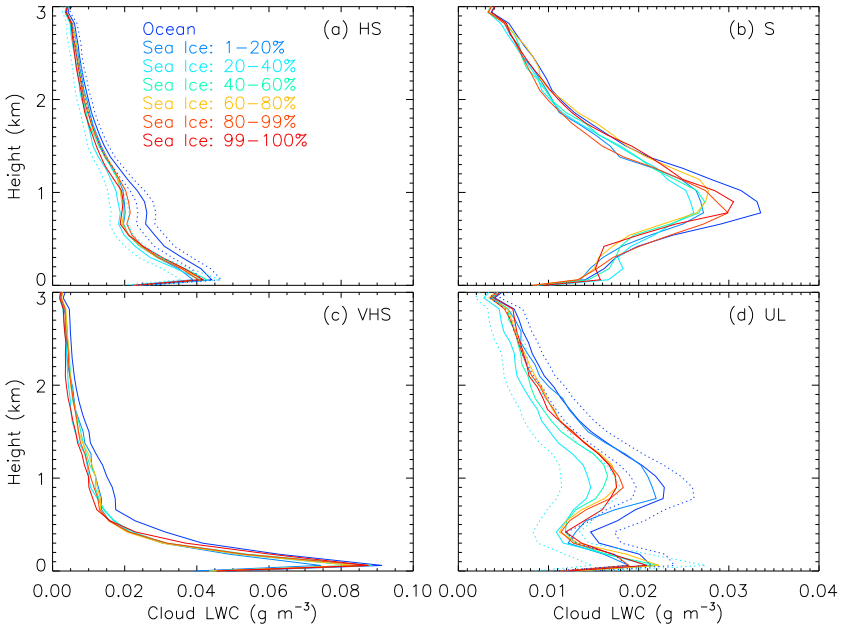

Figure 11. Summer season composite analysis applied to the LWC vertical profile for the (a) HS, (b) S, (c) VHS, and (d) UL regimes. Dashed lines represent the error and are the 2σ standard error for the average at each height. Error bars are only shown in cases where statistically significant differences are found.

Despite general agreement in the sign and magnitude of the covariance between the CF vertical profile and SIC, only a few regimes, seasons, and height ranges exhibit statistically significant differences (Table 4). The HS regime exhibits statistically significant differences in the average CF between the 0% and 20–40% SIC bins in all seasons. The height ranges at which the statistically significant differences occur are lower in summer (100–300 m) than in fall and winter (600–1000 m). The S regime exhibits statistically significant differences

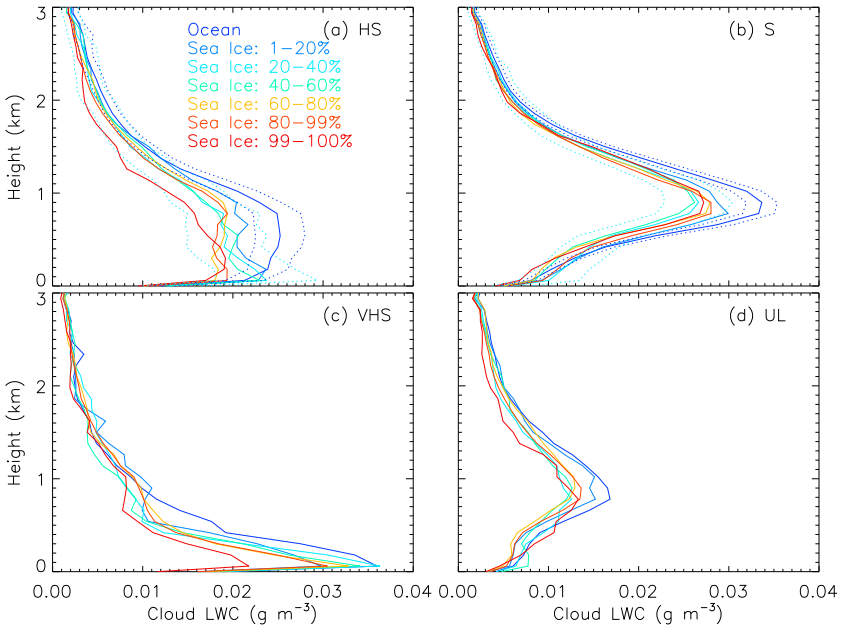

Figure 12. Fall season composite analysis applied to the LWC vertical profile for the (a) HS, (b) S, (c) VHS, and (d) UL regimes. Dashed lines represent the error and are the 2σ standard error for the average at each height. Error bars are only shown in cases where statistically significant differences are found.

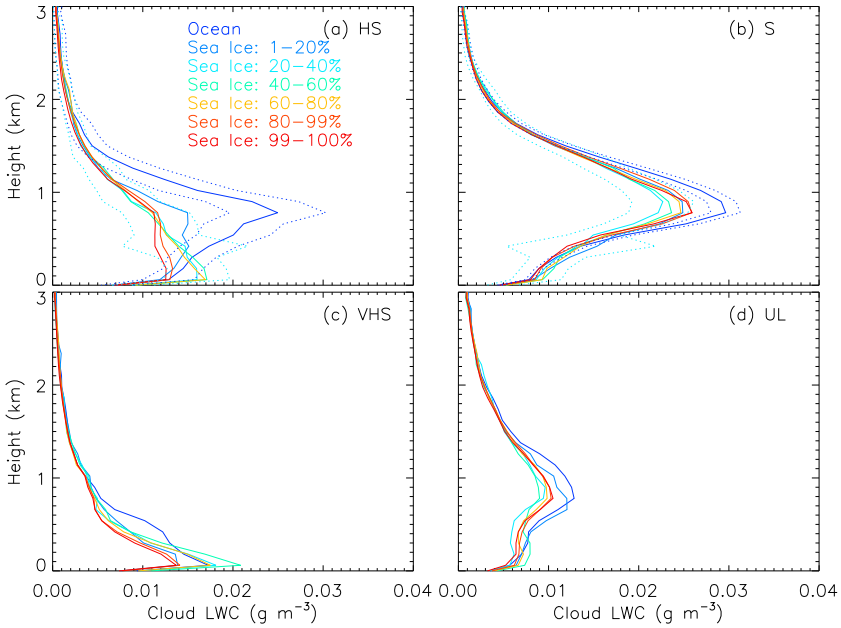

Figure 13. Winter season composite analysis applied to the LWC vertical profile for the (a) HS, (b) S, (c) VHS, and (d) UL regimes. Dashed lines represent the error and are the 2σ standard error for the average at each height. Error bars are only shown in cases where statistically significant differences are found.

at heights 600 m–1.1 km in fall and winter but not in summer. The UL regime shows no statistically significant differences at any vertical level in summer and winter; however, the CF vertical profile differences in fall reach 0.05 between 500 m and 1 km and the 0% and 40–60% SIC bins and are statistically significant. The average CF differences in the VHS regime reach 0.07 below 400 m in fall but are not statistically significant. The HS regime is the only regime that shows statistically significant differences in average CF (~0.05–0.07) for all seasons.

The primary difference in the CF vertical profile and SIC covariance between regimes is the height at which the CF change occurs not the magnitude. The height of maximum CF change coincides with the level of maximum average CF, which depends on LTS (Figure 2). As a result, the largest change in the average CF vertical profiles is found at a lower height in VHS than the S and HS regimes. The maximum CF change is similar for the HS, S, and VHS regimes.

4.2.2. Cloud Water Concentration Profile

The overall LWC profile covariance results are illustrated for each season in Figures 11–13. Most regimes and seasons exhibit smaller average LWC values in footprints with larger SIC. As with the average CF vertical profile, statistically significant decreases in LWC are found between 0% and 20–40% SIC and/or the 0% and 40–60% SIC between 500 m and 1.2 km. The decreases are most prominent at the height of the maximum LWC.

The overall magnitude of the average LWC vertical profile covariance varies by regime and season. As with the CF vertical profile, the magnitude of the average LWC covariance with SIC is quantified as the difference between the 0% and the 20–40% SIC. The largest change, reaching 0.015 g m^{-3} (~60% of the average LWC at 0% SIC), in the LWC is found in the HS regime in winter (Figure 13) near 800 m. This LWC change is attributed to a lowering of the height of the maximum LWC between 0% and 20–40% SIC. In the S regime, the average LWC at the level of maximum decreases between 0.007 and 0.008 g m^{-3} (~20–25% of the 0% SIC value) for all seasons between 600 and 1000 m. In the VHS regime, the LWC profile differences between 0% and 20–40% SIC are small in all seasons < 0.001 g m^{-3}; however, larger differences are found at higher SIC (Figure 12). The magnitude of the changes in the average LWC value in the UL regime reaches 0.009 g m^{-3} in summer and is 0.005 g m^{-3} in fall and winter.

The season when the largest differences occur depends upon atmospheric state regime. The largest differences between the 0% and 20–40% SIC are found in fall for the VHS and S regime. The HS regime shows the largest difference in winter, whereas the UL regime shows the largest difference in summer.

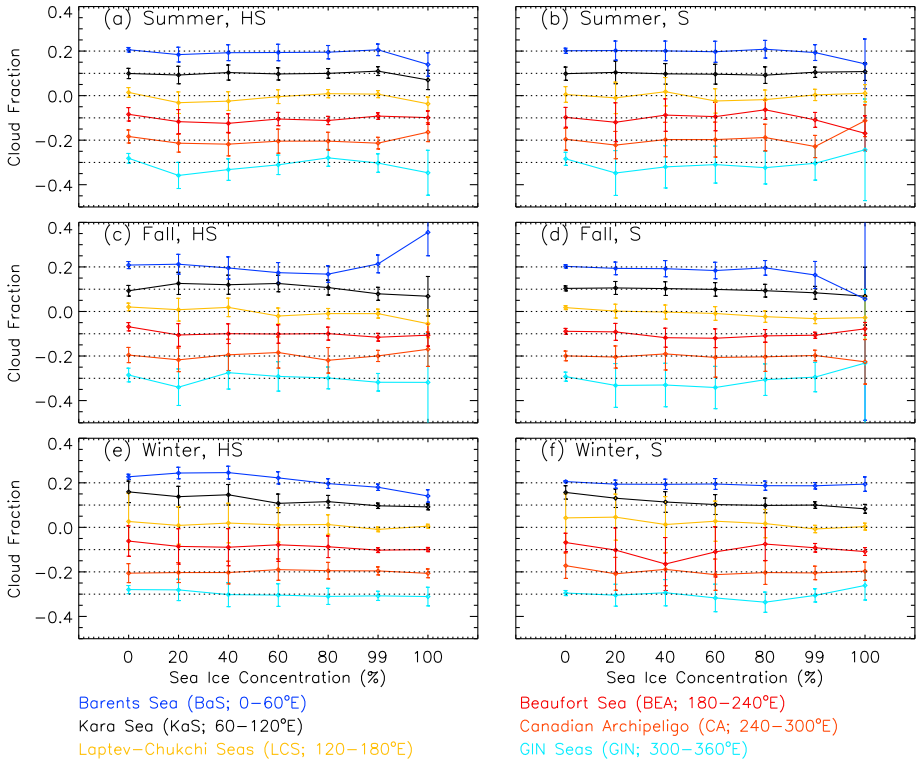

Figure 14. Regional cloud fraction anomalies in the lowest 3 km composited by SIC for the HS and S regime in all seasons: (a) summer, HS regime, (b) summer, S regime, (c) fall, HS regime, (d) fall, S regime, (e) winter, HS regime, and (f) winter S regime. Error bars represent the 2σ standard error for each average. Each bin is plotted by the upper SIC limit. To aid interpretation, each region is offset from each other by 0.1.

Few regimes, seasons, and height ranges exhibit statistically significant differences. The HS regime exhibits statistically significant differences in the average LWC in all seasons between the 0% and 20–40% SIC from 300 m to 1.1 km in summer, 800 m to 1.0 km in fall, and 500 m to 1.2 km in winter. The S regime exhibits statistically significant differences between 700 m and 1.1 km in fall and winter but none in summer. Statistically significant differences are not found in the VHS regime in any season. The UL regime exhibits a statistically significant change in the average LWC from 600 m to 1.2 km in summer but none in fall and winter. These height ranges, seasons, and regimes are similar to those found for the CF vertical profile covariance (Table 4).

The covariance in the average IWC profile with SIC is similar to LWC. Overall, the results indicate that the average IWC profile (not shown) exhibits smaller values at larger SIC in summer and winter but larger IWC values in fall (not shown). The IWC results exhibit more noise and only show a statistically significant difference in the S regime in winter. The magnitude of the differences between the 0% and 20–40% SIC of the average IWC profile is generally less than LWC except in a few seasons. In summer, the differences in the average IWC profile are less than 0.001 g m^{-3} in the HS and VHS regimes. Both the S and UL regimes indicate a decrease in IWC between the 0% and 20–40% SIC values. The magnitude of these changes is $<$0.004 g m^{-3} ($<$30% of the average IWC value at the level of maximum). In winter, all regimes exhibit a general decrease in average IWC profile.

4.3. Regional Analysis

Cloud properties show significant regional variations by atmospheric regime (Figure 3). Further, the probability distribution of SIC values (Figure 4) and the distribution of atmospheric regimes vary by region and season (Figure 5). Therefore, sampling differences from the SIC and atmospheric regime distributions across the regions may influence the Arctic domain averaged results. For instance, in winter the North Atlantic regions (e.g., GIN and BaS) have the most footprints with 0% SIC and exhibit a strong influence on the average cloud properties for the 0% SIC bin. A regional analysis of the cloud property covariance is, therefore, warranted to indicate the robustness of the Arctic domain average result.

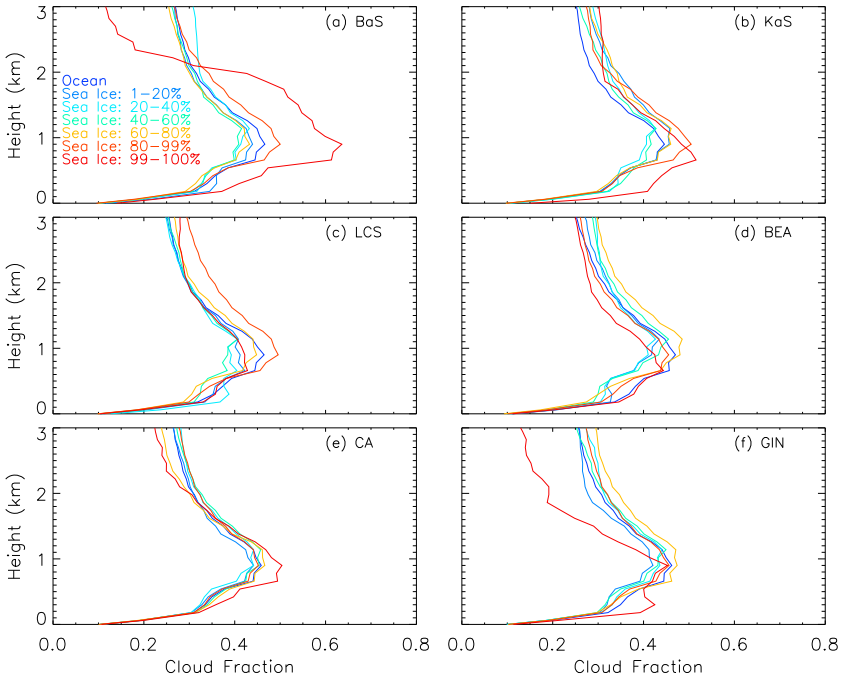

Figure 15. Fall season composite analysis applied to the CF vertical profile for six Arctic regions (a) BaS, (b) KaS, (c) LCS, (d) BEA, (e) CA, and (f) GIN.

This section discusses the main features of the regional variations in the covariance between cloud properties and SIC in the six Arctic regions. A notable feature of the regional results is the much larger error bars compared to the Arctic domain results because there are fewer samples. A longer data record is needed to more tightly constrain the regional covariance between cloud properties and SIC. The two primary results from the

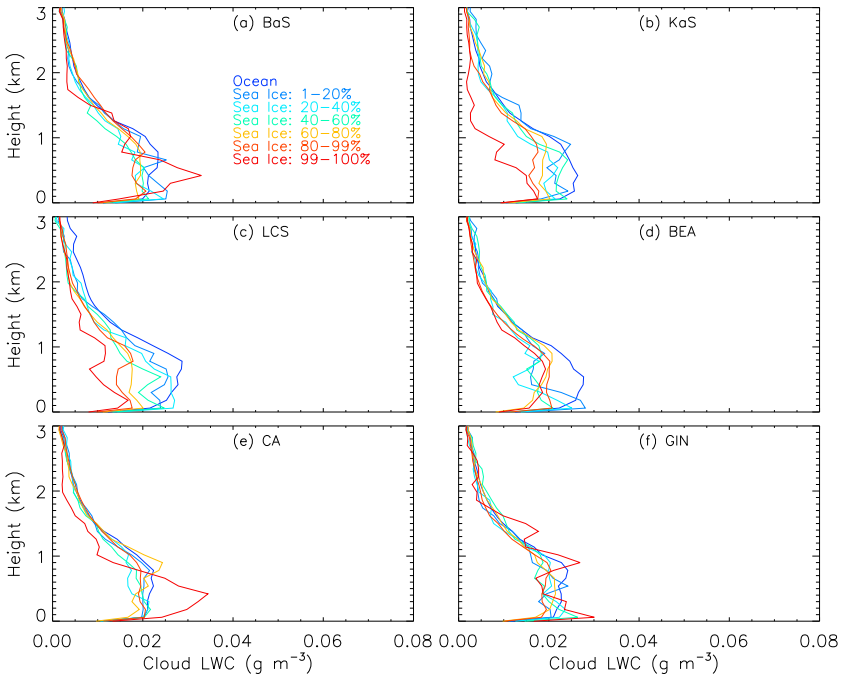

Figure 16. Fall season composite analysis applied to the LWC vertical profile for six Arctic regions (a) BaS, (b) KaS, (c) LCS, (d) BEA, (e) CA, and (f) GIN.

regional analysis are (1) only small deviations from the Arctic domain average results are found and (2) the region exhibiting the largest covariance varies seasonally. These points are true for all cloud properties.

Regional variability of the covariance between CF and SIC is summarized in Figure 14. To aid interpretation, each region in Figure 14 is offset from each other by ±0.1. In summer, the largest-magnitude covariance between CF and SIC reaching 0.07 is found in the S regime in BEA (Figure 14b). However, the LCS region in the HS regime (Figure 14a) exhibits the only statistically significant difference in summer reaching 0.05. The largest differences in fall (Figures 14c and 14d) are also found in LCS, reaching 0.05 and 0.07 in the HS and S regimes, respectively. The largest-magnitude covariance between CF and SIC in winter is found in BaS and KaS reaching 0.07 and 0.05, respectively, in the HS regime (Figures 14e and 14f); these differences are statistically significant. The seasonality of the regional variation in the CF and SIC covariance is attributed in part to the seasonal variation in SIC (Figure 4). This indicates a portion of the regional and seasonal variation of the CF, and SIC covariance is explained by the seasonal distribution of SIC.

The regions exhibiting the largest seasonal covariance of the CF and LWC vertical profiles with SIC are the same as the column-integrated CF. The LCS and BEA regions exhibit the largest covariance in summer and fall but in the BaS and KaS regions in winter. The regional variations in the CF and LWC vertical profile results for the HS regime are summarized in Figures 15 and 16 in fall. The HS regime in fall exhibits smaller average CF between 500 and 900 m at higher SIC values with the largest decreases found in LCS and BEA; these changes in CF between 500 and 900 m are between 0.05 and 0.08. In fall, the largest covariance in the average LWC profile below 1 km is found in KaS, LCS, and BEA. The CF and LWC vertical profile covariance results exhibit the largest differences in winter again in BaS and KaS (not shown) where the CF vertical profile difference between 0% and 40–60% SIC in KaS exceeds 0.1 between 600 and 900 m in the HS regime.

5. Discussion

We investigate the relationship between low-level CF, LWP, and IWP, with SIC, separated by season and atmospheric state over the Arctic. Atmospheric state is separated into four regimes depending on LTS and ω_{500}. CF and LWP increase with decreasing atmospheric stability below 3 km although the cloud top height increases with decreasing stability. This result corroborates the finding of *Solomon et al*. [2011] and *Barton et al*. [2012]. This relationship between CF and LWP and atmospheric stability in the Arctic is opposite of that for subtropical stratocumulus [*Wood*, 2012]. One possible reason for this is that the surface and atmospheric coupling is maintained even when cloud top height is increased in the Arctic. Additionally, increased LTS reduces the mixing between the free troposphere and cloud layer contributing to decreased CF and LWP because the free troposphere often serves as a moisture source for Arctic low clouds [*Solomon et al*., 2011; *Morrison et al*., 2012]. In subtropical stratocumulus, however, the free troposphere is a moisture sink.

Several statistically significant but weak in magnitude results are found. CF and LWP generally decrease with increasing SIC largely in agreement with previous work [*Schweiger et al*., 2008; *Kay and Gettelman*, 2009; *Eastman and Warren*, 2010; *Palm et al*., 2010; *Cuzzone and Vavrus*, 2011; *Barton et al*., 2012; *Sato et al*., 2012]. The decrease is statistically significant in the HS regime in each season. Statistically significant differences in the average CF and LWC vertical profiles are also found in the HS regime. The CF and LWC vertical profiles do not change uniformly with height, but rather, the largest changes are found at the level of the maximum cloud property. The largest and statistically significant changes in the CF and LWC vertical profiles are consistently found at heights between 500 m and 1.2 km, which contain the level of the maximum cloud property. A decrease in the height of the average maximum CF is not indicated by these results. This is true for all regimes suggesting that the increased cloud height under reduced SIC described by *Schweiger et al*. [2008] and *Sato et al*. [2012] may result from a change in atmospheric state (e.g., from HS to S regime). This behavior also describes the atmospheric regime differences in the cloud property vertical profile covariance with SIC, as the level of maximum CF or LWC decreased with increasing LTS (e.g., from S to VHS).

Our overall results are consistent with *Barton et al*. [2012] indicating that the CF vertical profile covariance with SIC depends upon the atmospheric dynamic and thermodynamic conditions. The results show that the magnitude of changes in CF and LWC with atmospheric regime is generally larger than the cloud property covariance with SIC. Therefore, analysis of the CF and SIC relationship not considering the influence of atmospheric regime can be misleading.

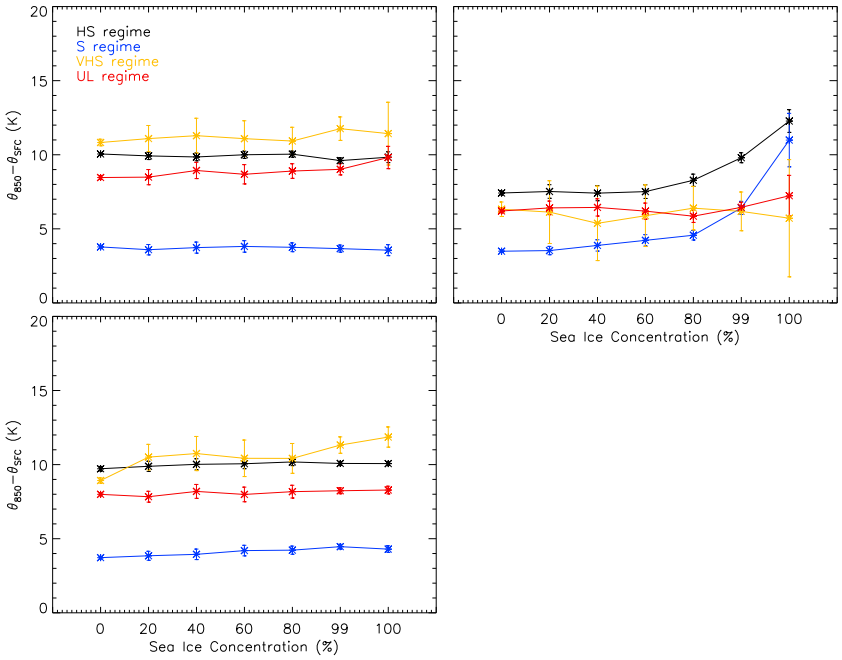

Figure 17. Average near-surface static stability, defined as θ_{850}–θ_{SFC}, composited by SIC for each atmospheric regime and season: (a) JJA, (b) SO, and (c) NDJFMAM. Error bars represent the 2σ standard error for each average. Each bin is plotted by the upper SIC limit.

Previous work suggests that the CF response to sea ice may vary seasonally. *Kay and Gettelman* [2009] demonstrate a previously undocumented seasonal shift in the cloud response to sea ice finding a stronger relationship between CF and sea ice in autumn and no relationship in summer. We also find that the magnitude of the cloud property covariance with SIC varies seasonally in agreement with *Kay and Gettelman* [2009]. The largest CF changes with SIC are found in fall and are weakest in winter. Our results, however, indicate a statistically significant covariance between cloud properties and SIC in summer in the HS regime. The covariance between CF and LWP in summer is relatively weak for CF, < 0.03, but larger for LWP reaching 7 g m^{-2} between 0% and 20–40% SIC. It should be noted, however, that while this increase in LWP is physically consistent with theoretical simulations, the scene/surface type-dependent uncertainty in passive water path retrievals is larger than 7 g m^{-2} (P. Minnis, personal communication, 2015).

Kay and Gettelman [2009] postulate that the seasonal variability in the cloud response to sea ice results from the seasonality of near-surface static stability where weaker stability in autumn promotes a stronger atmosphere-surface coupling. Figure 17, however, indicates a weak seasonal variation in near-surface static stability, defined as θ_{850}–θ_{SFC}, within each regime inconsistent with *Kay and Gettelman* [2009]. Rather, the fall season exhibits a significant covariance between near surface static stability and SIC, especially for the HS and S regimes. We hypothesize that the large covariance in fall between cloud properties and SIC results from the increase in near-surface static stability with increased SIC causing the cloud and surface layers to quickly become decoupled. Near-surface static stability obtained from reanalysis is not well constrained, but the seasonal variation is striking.

To the best of the authors' knowledge no formal observational investigations of the relationship between sea ice and cloud properties in winter are found in the literature—likely due to the large uncertainty in passive cloud retrievals. This analysis provides a first indication that the Arctic domain covariance between cloud properties and SIC is weakest in winter. This result is inconsistent with climate model studies suggesting the strongest cloud response to sea ice in winter [*Vavrus et al.*, 2011] and may have significant implications to Arctic cloud feedback.

Among regimes used in this study, the UL is the only atmospheric regime characterized by rising vertical motion in the midtroposphere and represents frontal clouds. Our results show large differences in the average CF and LWC vertical profiles with varying SIC, but consistent or statistically significant changes in cloud

properties are rarely found in the UL regime. The results suggest a potential influence of SIC on low cloud properties within the UL regime only in the LCS and BEA regions. Consistent with *Kay and Gettelman* [2009], no Arctic domain-wide frontal cloud response to sea ice is found. This suggests that local atmosphere-surface coupling processes do not play a major role in determining cloud properties of frontal clouds.

At this time, we cannot confidently say that the change in the average cloud properties at varying SIC values is solely due to the influence of SIC on the surface turbulent fluxes. Several limiting factors are identified.

The atmospheric state regimes from *Barton et al*. [2012] do not account completely for the meteorological influence on cloud properties (Figure 3). This is not addressed in *Barton et al*., 2012]. The regional dependence may not be evident in their results because only CALIOP data are used; their results are implicitly subset regionally. We speculate that the influence of regional meteorological variability is more apparent in our study because CloudSat penetrates thicker cloud when CALIOP is attenuated in regions such as the North Atlantic, which has significantly different meteorology than other Arctic regions. A regionally robust sorting of clouds by meteorology and longer data record is needed to reduce the noise in the regional results.

Knowledge of atmospheric conditions is another factor-limiting confidence in the results. Meteorological reanalysis is poorly constrained in the Arctic. The atmospheric regimes in this study are based on MERRA, and it is possible that the footprints are classified incorrectly. The sensitivity of the study results to reanalysis is tested with ERA-Interim, and the reanalysis is determined to have little influence on the results. However, the reanalysis meteorological state information may add noise to the results obscuring some relationships. A strong relationship is indicated here between the level of maximum average CF (Figure 2) and LTS. In the future, a more robust methodology would be to sort directly by cloud properties (e.g., cloud top height).

Associated with the weaknesses in meteorological reanalysis, knowledge of whether an individual cloud is coupled or decoupled from the surface and further the magnitude of the latent and sensible heat fluxes is lacking. The approach adopted here is based upon the assumption of a correlation between cloud-surface coupling and LTS (e.g., atmospheric regimes). Based upon this assumption, the S regime should exhibit the strongest cloud-surface coupling because it exhibits the weakest near-surface static stability (Figure 17). However, the HS regime exhibits the largest-magnitude covariance between cloud properties and SIC suggesting a stronger coupling with the surface; the stronger covariance could also be caused by multiple other factors.

Another confounding factor in the relationship between clouds and SIC involves the relationship between LTS and SIC. As noted previously, low-level, surface-based temperature inversions occur frequently across the Arctic. The presence of surface-based temperature inversions are strongly linked to the characteristics of the Arctic surface radiation budget and surface sea ice characteristics [e.g., *Pavelsky et al*., 2011]. As a result, significant variability in Arctic LTS results from changes in the temporal and spatial variations in the surface energy budget [*Medeiros et al*., 2011; *Zhang et al*., 2011]. Specifically, *Pavelsky et al*. [2011] demonstrate a significant positive correlation between sea ice and Arctic inversion strength—larger SIC and larger LTS —confounding the present results (e.g., Figure 17). However, the covariance between SIC and LTS within each atmospheric regime is weak (not shown). Future work is needed to unravel the relationship between clouds, SIC, and LTS.

Overall, our interpretation of the small average cloud covariance with sea ice is that cloud layers are likely frequently decoupled from the surface, and as a result, there is little influence of sea ice on cloud characteristics. This does not mean that strong cloud-sea ice interactions do not occur. It is clearly shown with cloud models that the buoyant circulation of a cloud is enhanced by an additional surface turbulent heat flux increasing the updraft speed and total water content. The results suggest that this process is not as critical to determining observed average Arctic cloud characteristics as implied by climate models [e.g., *Vavrus et al*., 2009; *Kay et al*., 2010]. Recently, *Solomon et al*. [2014] using idealized large eddy simulation experiments suggest that equilibrium cloud properties may be independent of cloud-surface layer coupling in the presence of an above cloud moisture inversion, which supports our interpretation.

6. Conclusion

This paper provides a refined perspective of the relationship between Arctic low cloud properties and sea ice using a satellite footprint-level quantification of Arctic low cloud property changes with sea ice concentration

using active remote sensing satellite data from the NASA A-Train. The relationship between Arctic low cloud properties and sea ice concentration are determined by first partitioning each footprint into four atmospheric state regimes defined by thresholds of lower tropospheric stability and 500 hPa vertical velocity yielding several results.

A strong dependence of cloud properties on the lower tropospheric stability and midtropospheric vertical velocity is found. Increased lower tropospheric stability is associated with decreases in low cloud fraction, cloud liquid water, cloud ice water, and cloud total water. The cloud property vertical profiles also depend on lower tropospheric stability where the height of the maximum cloud fraction and liquid water content decreases with increasing stability.

A statistically significant covariance is found between cloud fraction and cloud liquid water and their vertical distributions with sea ice concentration in several atmospheric regimes and seasons, primarily when lower tropospheric stability is between 16 and 24 K. The general characteristics of the relationship between surface to 3 km column-integrated cloud fraction and liquid water path are such that each cloud property tends to decrease at higher sea ice concentrations. The relationship between ice water path and SIC indicates a more complicated relationship. The magnitude and structure of the cloud property relationship with SIC are shown to depend upon atmospheric condition and season.

Cloud properties are found overall to vary more between two atmospheric regimes than with sea ice concentration. However, the covariance between LWP and SIC in fall is of similar magnitude to the average LWP differences between the HS and S regimes. This result indicates that one must consider stratifying by atmosphere conditions to find a reliable and robust relationship between clouds and SIC.

The regional analysis indicates that several regions, namely, the Laptev, Chukchi, and Beaufort Seas, exhibit the largest regional covariance between cloud properties and sea ice in summer and fall. The Barents and Kara Sea regions exhibit the largest in winter. The distribution of SIC may be a critical factor influencing the regional covariance between clouds and sea ice. This implies that under certain atmospheric conditions modeling the distribution of sea ice within the marginal ice zone may be important for Arctic climate. However, a longer data record is needed to refine this result.

Acknowledgments
The authors would like to thank the three anonymous reviewers of this manuscript for their insightful comments significantly improving this manuscript. This work is funded by the NASA Interdisciplinary Studies Program grant NNH12ZDA001N-IDS. The processing of the C3M data used in this analysis was funded under the NASA Energy and Water Cycle Studies program and is available from the Langley Atmospheric Science Data Center (http://eosweb.larc.nasa.gov).

References

Austin, R. T., A. J. Heymsfield, and G. L. Stephens (2009), Retrieval of ice cloud microphysical parameters using the CloudSat millimeter-wave radar and temperature, *J. Geophys. Res.*, *114*, D00A23, doi:10.1029/2008JD010049.

Avery, M., et al. (2012), Cloud ice water content retrieved from the CALIOP space-based lidar, *Geophys. Res. Lett.*, *39*, L05808, doi:10.1029/2011GL050545.

Barton, N. P., and D. E. Veron (2012), Response of clouds and surface energy fluxes to changes in sea-ice cover over the Laptev Sea (Arctic Ocean), *Clim. Res.*, *54*, 69–84, doi:10.3354/cr01101.

Barton, N. P., S. A. Klein, J. S. Boyle, and Y. Y. Zhang (2012), Arctic synoptic regions: Comparing domain-wide Arctic cloud observations with CAM4 and CAM5 during similar dynamics, *J. Geophys. Res.*, *117*, D15205, doi:10.1029/2012JD017589.

Berrisford, P., et al. (2011), The ERA-Interim archive version 2.0. ERA report series. 1. Technical report European Centre for Medium-Range Weather Forecasts, Shinfield Park, Reading. 23 pp.

Boisvert, L. N., T. Markus, C. L. Parkinson, and T. Vihma (2012), Moisture fluxes derived from EOS aqua satellite data for the North Water polynya over 2003–2009, *J. Geophys. Res.*, *117*, D06119, doi:10.1029/2001JD016949.

Bourassa, M. A., et al. (2013), High-latitude ocean and se ice surface fluxes: Challenges for climate research, *Bull. Am. Meteorol. Soc.*, doi:10.1175/BAMS-D-11-00244.1.

Cavalieri, D. J., C. L. Parkinson, P. Gloersen, and H. Zwally (1996), *Sea Ice Concentrations from Nimbus-7 SMMR and DMSP SSM/I-SSMIS Passive Microwave Data Updated Yearly*, NASA Natl. Snow Ice Data Cent. Distrib. Act. Arch. Cent., Boulder, Colo., doi:10.5067/8GQ8LZQVL0VL.

Cavalieri, D. J., C. l. Parkinson, P. Gloersen, and H. J. Zwally (1997), Arctic and Antarctic sea ice concentrations from multichannel passive-microwave satellite data sets: October 1978 to December 1996, User's Guide, NASA Technical Memorandum 104647. 17 pages.

Cesana, G., J. E. Kay, H. Chepfer, J. M. English, and G. de Boer (2012), Ubiquitous low-level liquid-containing Arctic clouds: New observations and climate model constraints from CALIPSO-GOCCP, *Geophys. Res. Lett.*, *39*, L20804, doi:10.1029/2012GL053385.

Chylek, P., C. K. Folland, G. Lesins, M. K. Dubey, and M.-Y. Wang (2009), Arctic air temperature change amplification and the Atlantic multidecadal oscillation, *Geophys. Res. Lett.*, *36*, L14801, doi:10.1029/2009GL038777.

Comiso, J. C., C. L. Parkinson, R. Gersten, and L. Stock (2008), Accelerated decline in the Arctic sea ice cover, *Geophys. Res. Lett.*, *35*, L01703, doi:10.1029/2007GL031972.

Curry, J. A., W. B. Rossow, D. Randall, and J. L. Schramm (1996), Overview of Arctic cloud and radiation characteristics, *J. Clim.*, *9*, 1731–1762.

Cuzzone, J., and S. Vavrus (2011), The relationships between Arctic sea ice and cloud-related variables in the ERA-Interim reanalysis and CCSM3, *Environ. Res. Lett.*, *6*, doi:10.1088/1748-9326/6/1/014016.

de Boer, G., G. J. Tripoli, and E. W. Eloranta (2008), Preliminary comparison of CloudSAT-derived microphysical quantities with ground-based measurements for mixed-phase cloud research in the Arctic, *J. Geophys. Res.*, *113*, D00A06, doi:10.1029/2008JD010029.

Dee, D. P., et al. (2011), The ERA-Interim reanalysis: Configuration and performance of the data assimilation system, *Q. J. R. Meteorol. Soc.*, *137*, 553–597.

Eastman, R., and S. G. Warren (2010), Interannual variations of Arctic cloud types in relation to sea ice, *J. Clim.*, *23*, 4216–4232.

Fu, Q. (1996), An accurate parameterization of the solar radiation properties of cirrus clouds for climate models, *J. Clim.*, *9*, 2058–2082.
Gordon, N. D., J. R. Norris, C. P. Weaver, and S. A. Klein (2005), Cluster analysis of cloud regimes and characteristic dynamics of midlatitude synoptic systems in observations and a model, *J. Geophys. Res.*, *110*, D15S17, doi:10.1029/2004JD005027.
Hall, A. (2004), The role of surface albedo feedback in climate, *J. Clim.*, *17*, 1500–1568.
Herman, G., and R. Goody (1976), Formation and persistence of summertime Arctic stratus clouds, *J. Atmos. Sci.*, *33*, 1537–1553.
Holland, M. M., and C. Bitz (2003), Polar amplifications of climate change in coupled models, *Clim. Dyn.*, *21*, 221–232.
Kato, S., N. G. Loeb, P. Minnis, J. A. Francis, T. P. Charlock, D. A. Rutan, E. E. Clothiaux, and S. Sun-Mack (2006), Seasonal and interannual variation of top-of-atmosphere irradiance and cloud cover over polar regions derived from the CERES data set, *Geophys. Res. Lett.*, *33*, L19804, doi:10.1029/2006GL026685.
Kato, S., S. Sun-Mack, W. F. Miller, F. G. Rose, Y. Chen, P. Minnis, and B. A. Wielicki (2010), Relationships among cloud occurrence frequency, overlap, and effective thickness derived from CALIPSO and CloudSat merged cloud vertical profiles, *J. Geophys. Res.*, *115*, D00H28, doi:10.1029/2008JD012277.
Kato, S., et al. (2011), Improvements of top-of-atmosphere and surface irradiance computations with CALIPSO-, CloudSat-, and MODIS-derived cloud and aerosol properties, *J. Geophys. Res.*, *116*, D19209, doi:10.1029/2011JD016050.
Kay, J. E., and A. Gettelman (2009), Cloud influence on and response to seasonal Arctic sea ice loss, *J. Geophys. Res.*, *114*, D18204, doi:10.1029/2009JD011773.
Kay, J. E., and T. L'Ecuyer (2013), Observational constraints on Arctic ocean clouds and radiative fluxes during the early 21st century, *J. Geophy. Res. Atmos.*, *118*, 7219–7236, doi:10.1002/jgrd.50489.
Kay, J. E., T. L'Ecuyer, A. Gettelman, G. Stephens, and C. O'Dell (2008), The contribution of cloud and radiation anomalies to the 2007 Arctic sea ice extent minimum, *Geophys. Res. Lett.*, *35*, L08503, doi:10.1029/2008GL033451.
Kay, J. E., K. Raeder, A. Gettelman, and J. Anderson (2010), The boundary layer response to recent Arctic sea ice loss and implications for high-latitude climate feedbacks, *J. Clim.*, *24*, 428–447.
Li, Y., D. W. J. Thompson, G. L. Stephens, and S. Bony (2014), A global survey of the instantaneous linkages between cloud vertical structure and large-scale climate, *J. Geophys. Res. Atmos.*, *119*, 3770–3792, doi:10.1002/2013JD020669.
Manabe, S., and R. T. Wetherald (1975), The effects of doubling the CO_2 concentration on the climate of a general circulation model, *J. Atmos. Sci.*, *32*, 3–15.
Marchand, R. T., G. Mace, T. Ackerman, and G. Stephens (2008), Hydrometeor detection using CloudSat—An Earth orbiting 94 GHz cloud radar, *J. Atmos. Oceanic Technol.*, *25*, 519–533.
Medeiros, B., C. Deser, R. A. Tomas, and J. E. Kay (2011), Arctic inversion strength in climate models, *J. Clim.*, *24*, 4733–4740.
Minnis, P., D. P. Garber, D. F. Young, R. F. Arduini, and Y. Takano (1998), Parameterization of reflectance and effective emittance for satellite remote sensing of cloud properties, *J. Atmos. Sci.*, *55*, 3313–3339.
Minnis, P., et al. (2011a), CERES Edition 2 cloud property retrievals using TRMM VIRS and Terra and Aqua MODIS data: Part I: Algorithms, *IEEE Trans. Geosci. Remote Sens.*, *49*, doi:10.1108/TGRS.2011.2144602.
Minnis, P., et al. (2011b), CERES Edition 2 cloud property retrievals using TRMM VIRS and Terra and Aqua MODIS data: Part II: Examples of average results and comparisons with other data, *IEEE Trans. Geosci. Remote Sens.*, *49*, doi:10.1108/TGRS.2011.2144601.
Morrison, H., G. de Boer, G. Feingold, J. Harrington, M. D. Shupe, and K. Sulia (2012), Resilience of persistent Arctic mixed-phase clouds, *Nat. Geosci.*, *5*, 11–17, doi:10.1038/ngeo1332.
Palm, S. P., S. T. Strey, J. Spinhime, and T. Markus (2010), Influence of Arctic sea ice extent on polar cloud fraction and vertical structure and implications for regional climate, *J. Geophys. Res.*, *115*, D21209, doi:10.1029/2010JD013900.
Pavelsky, T. M., J. Boe, A. Hall, and E. J. Fetzer (2011), Atmospheric inversion strength over polar oceans in winter regulated by sea ice, *Clim. Dyn.*, *36*, 945–955.
Pinto, J. O. (1998), Autumnal mixed-phase cloudy boundary layers in the Arctic, *J. Atmos. Sci.*, *55*, 2016–2038.
Pistone, K., I. Eisenman, and V. Ramanathan (2014), Observational determination of albedo decrease caused by vanishing Arctic sea ice, *Proc. Natl. Acad. Sci. U.S.A.*, *111*(9), 3322–3326, doi:10.1073/pnas.1318201111.
Polyakov, I. V., J. E. Walsh, and R. Kwok (2012), Recent changes of Arctic multiyear sea ice coverage and the likely causes, *Bull. Am. Meteorol. Soc.*, doi:10.1175/BAMS-D-11-0000.1.
Rienecker, M. M., et al. (2011), MERRA: NASA's Modern-Era Retrospective Analysis for Research and Applications, *J. Clim.*, *24*, 3624–3648.
Rigor, I. G., R. L. Colony, and S. Martin (2000), Variations in surface air temperature observations in the Arctic, 1979–1997, *J. Clim.*, *13*(5), 896–914.
Sassen, K., and Z. Wang (2008), Classifying clouds around the globe with the CloudSat radar: 1-year of results, *Geophys. Res. Lett.*, *35*, L04805, doi:10.1029/2007GL032591.
Sato, K., J. Inoue, Y.-M. Kodama, and J. E. Overland (2012), Impact of Arctic sea-ice retreat on the recent change in cloud-base height during autumn, *Geophys. Res. Lett.*, *39*, L10503, doi:10.1029/2012GL051850.
Schweiger, A. J., S. W. Lindsay, S. Vavrus, and J. A. Francis (2008), Relationships between Arctic sea ice and clouds during autumn, *J. Clim.*, *21*, 4799–4811.
Sejas, S., M. Cai, A. Hu, J. Meehl, W. Washington, and P. C. Taylor (2014), On the seasonality of polar warming amplification, *J. Clim.*, *27*, 5653–5669.
Serreze, M. C., and R. G. Barry (2011), Processes and impacts of Arctic amplification: A research synthesis, *Global Planet. Change*, *77*, 85–96, doi:10.1016/j.gloplacha.2011.03.004.
Shupe, M. D., and J. M. Intrieri (2004), Cloud radiative forcing of the Arctic surface: The influence of cloud properties, surface albedo, and solar zenith angle, *J. Clim.*, *17*, 616–628.
Shupe, M. D., P. O. G. Persson, I. M. Brooks, M. Tjernstrom, J. Sedlar, T. Mauritsen, S. Sjogren, and C. Leck (2013), Cloud and boundary layer interactions over the Arctic sea ice in late summer, *Atmos. Chem. Phys.*, *13*, 9379–9400, doi:10.5194/acp-13-9379-2013.
Solomon, A., M. D. Shupe, P. O. G. Persson, and H. Morrison (2011), Moisture and dynamical interactions maintaining decoupled Arctic mixed-phase stratocumulus in the presence of a humidity inversion, *Atmos. Chem. Phys.*, *11*, 10,127–10,148, doi:10.5194/acp-11-10127-2011.
Solomon, A., et al. (2014), The sensitivity of springtime Arctic mixed-phase stratocumulus clouds to surface-layer and cloud-top inversion-layer moisture sources, *J. Atmos. Sci.*, *71*, 574–595.
Steffen, K., D. J. Cavalieri, J. C. Comiso, K. S. Germain, P. Gloersen, J. Key, and I. Rubinstein (1992), The estimation of geophysical parameters using passive microwave algorithms. in *Microwave Remote Sensing of Sea Ice*, edited by F. Carsey, chap. 10, 243–259, AGU, Washington, D. C.
Stephens, G. L., et al. (2008), CloudSat mission: Performance and early science after the first year of operation, *J. Geophys. Res.*, *113*, D00A18, doi:10.1029/2008JD009982.

Stroeve, J., M. M. Holland, W. Meier, T. Scambos, and M. Serreze (2007), Arctic sea ice decline: Faster than forecast, *Geophys. Res. Lett.*, *34*, L09501, doi:10.1029/2007GL029703.

Taylor, P. C. (2012), The role of clouds: An introduction and rapporteur report, *Surv. Geophys.*, *33*, 1–9, doi:10.1007/s107-12-012-9182-2.

Taylor, P. C., R. G. Ellingson, and M. Cai (2011a), Geographic distribution of climate feedbacks in the NCAR CCSM3.0, *J. Clim.*, *24*, 2737–2753, doi:10.1175/2010JCLI3788.1.

Taylor, P. C., R. G. Ellingson, and M. Cai (2011b), Seasonal distribution of climate feedbacks in the NCAR CCSM3.0, *J. Clim.*, *24*, 3433–3444, doi:10.1175/2011JCLI3862.1.

Taylor, P. C., M. Cai, A. Hu, J. Meehl, W. Washington, and G. J. Zhang (2013), A decomposition of feedback contributions to polar warming amplification, *J. Clim.*, *26*, 7023–7043, doi:10.1175/JCLI-D-12-00696.1.

Vavrus, S., D. Waliser, A. Schweiger, and J. Francis (2009), Simulations of 20th and 21st century Arctic cloud amount in the global climate models assessed in the IPCC AR4, *Clim. Dyn.*, *33*, 1099–1115, doi:10.1007/s00382-008-0475-6.

Vavrus, S., U. S. Bhatt, and V. A. Alexeev (2011), Factors influencing simulated changes in future Arctic cloudiness, *J. Clim.*, *24*, 4817–4830.

Wang, X., and J. R. Key (2003), Recent trends in Arctic surface, cloud, and radiation properties from space, *Science*, *299*, 1725–1728, doi:10.1126/science.1078065.

Wielicki, B. A., B. R. Barkstrom, E. F. Harrison, R. B. Lee III, G. L. Smith, and J. E. Cooper (1996), Clouds and the Earth's Radiant Energy System (CERES): An Earth observing system experiment, *Bull. Am. Meteorol. Soc.*, *77*, 853–868.

Winker, D. M., W. H. Hunt, and M. J. McGill (2007), Initial performance assessment of CALIOP, *Geophys. Res. Lett.*, *34*, L19803, doi:10.1029/2007GL030135.

Wood, R. (2012), Stratocumulus clouds, *Mon. Weather Rev.*, *140*, 2373–2423.

Zhang, Y. H., D. J. Seidel, J. C. Golaz, C. Deser, and R. A. Tomas (2011), Climatological characteristics of Arctic and Antarctic surface-based inversions, *J. Clim.*, *24*, 5167–5186.